High-throughput assessment of the controllability of a nuclear-spin register coupled to a defect

Filippos Dakis,[1,2,*] Evangelia Takou[1,2,†] Edwin Barnes[1,2,‡] and Sophia E. Economou[1,2,§]

[1]*Department of Physics, Virginia Tech, Blacksburg, Virginia 24061, USA*

[2]*Virginia Tech Center for Quantum Information Science and Engineering, Blacksburg, Virginia 24061, USA*

Quantum memories play a key role in facilitating tasks within quantum networks and quantum information processing, including secure communications, advanced quantum sensing, and distributed quantum computing. Progress in characterizing large nuclear-spin registers coupled to defect electronic spins has been significant, but selecting memory qubits remains challenging due to the multitude of possible assignments. Numerical simulations for evaluating entangling gate fidelities encounter obstacles, restricting research to small registers, while experimental investigations are time-consuming and often limited to well-understood samples. Here we present an efficient methodology for systematically assessing the controllability of defect systems coupled to nuclear-spin registers. We showcase the approach by investigating the generation of entanglement links between silicon monovacancy or divacancy centers in SiC and randomly selected sets of nuclear spins within the two-species (^{13}C and ^{29}Si) nuclear register. We quantify the performance of entangling gate operations and present the achievable gate fidelities, considering both the size of the register and the presence of unwanted nuclear spins. We find that some control sequences perform better than others depending on the number of target versus bath nuclei. This efficient approach is a guide for both experimental investigation and engineering, facilitating the high-throughput exploration of suitable defect systems for quantum memories.

I. INTRODUCTION

Solid-state defect systems are a leading platform for quantum networks, quantum sensing, and other quantum information processing tasks. Defects in diamond, such as nitrogen-vacancy (N-*V*) centers [1–3], silicon-vacancy (Si-*V*) centers [4,5], and tin-vacancy (Sn-*V*) centers [6,7], have been intensely studied and used for milestone demonstrations of building blocks for quantum networks. Similarly, various defects in silicon carbide (SiC) are explored for such tasks due to the host material's attractive properties and the more desirable emission frequencies compared to diamond defects. Among SiC defects, silicon vacancies [8–10] and neutral divacancy centers [11] are especially promising.

Considering the vast space of possible defects in a wide range of host materials, the community is taking steps toward a more systematic search for new defects with desirable properties using computational tools such as density-functional theory [12,13]. The latter predict optoelectronic and kinematic properties, which, while important, do not suffice in determining the suitability of a given defect for a particular quantum information processing task. The most fundamental missing element in such defect surveys is the evaluation of the *operational performance* of the defect as a qubit in a larger quantum register, typically composed of spinful isotopes in the host material. For example, in network applications, the electronic spin functions as the communication qubit due to its spin-photon interface, while nearby nuclear spins can serve as long-lived quantum memories needed for quantum repeaters [14–16]. In the case of diamond, for instance, the low but nonzero concentration of ^{13}C nuclei, together with their long coherence times, allows for the development of quantum memories for information storage and buffering. Such memory qubits are also often necessary for entanglement distillation [3] and quantum error-correction protocols [17], while they can also serve as a useful resource for quantum sensing [18–21].

However, assessing and controlling nuclear-spin memories in solid-state spin-defect platforms faces challenges on two fronts: (i) The nuclear spins are randomly situated at distant lattice sites, resulting in random hyperfine (HF) interactions that are weak compared to the defect

---

*Contact author: dakisfilippos@vt.edu

†Contact author: etakou@vt.edu

‡Contact author: efbarnes@vt.edu

§Contact author: economou@vt.edu

spin's dephasing rate. (ii) The HF interactions between nuclear spins and the electronic spin defect are always present (they cannot be switched off). Thankfully, dynamical decoupling (DD) pulse sequences offer a solution to both challenges [22]. In principle, all nuclear spins except a selected target one can be decoupled from the defect by tuning parameters associated with these DD sequences, particularly the interpulse spacings and the number of iterations of a basic sequence unit. By varying these control knobs, different nuclear spins across the total register can be selected. To date, impressive experiments have been conducted to characterize the register and demonstrate entangling quantum gates between defect and nuclear-spin qubits [4,5,11,18,22–24]. Moreover, this approach has initiated first steps toward distributing entanglement across a network of a few quantum nodes [1,25], implementing quantum repeater protocols [24], performing entanglement distillation [3], or realizing error-correction schemes [23,26,27]. Very recently, entanglement between nuclear-spin qubits coupled to two Si-*V* centers in diamond at opposite ends of a 40-km fiber was demonstrated [28].

Despite the significant progress in characterizing large nuclear-spin registers [19], selecting memory qubits from these registers remains inherently difficult due to the combinatorially large number of possible assignments. An important metric in this selection process is the quality of the gates for a given assignment. Unfortunately, numerical simulations to evaluate gate fidelity face significant hurdles, as they require solving for the time evolution of the many-body system, rendering such calculations prohibitively difficult for large registers. Consequently, only small-sized registers could be simulated so far. Although experimental investigations could partially alleviate this challenge, they are time-consuming, and academic labs often focus their investigations on a few well-understood and characterized samples and are not yet as concerned about questions of yield and scale.

In this paper, we address this challenge by establishing an efficient method for assessing the controllability of the total system consisting of the defect spin coupled to an arbitrary multinuclear-spin register. We do this by leveraging a recent formalism for characterizing multispin entanglement [29] that completely sidesteps the need to simulate many-body dynamics—a notoriously resource-intensive and time-consuming computational task. Our method enables one to rapidly and systematically identify suitable nuclear spins to use as memories, as well as optimal control sequences for manipulating them with high fidelity. While our method is general and can be applied to any defect, we showcase our approach with silicon monovacancy and divacancy defects in silicon carbide coupled to two species of nuclear spins, ^{13}C and ^{29}Si. These defects are especially promising for networks due to the fact that they emit at or near telecom bands. We determine how electron-multinuclear gate fidelities depend on the number of target versus bath nuclei. We compare the performance of several leading DD sequences in this task, finding that the relative performance depends on the sizes of the nuclear-spin memory register and the nuclear-spin bath. We further show that the sign difference in the gyromagnetic ratios of the two nuclear-spin species is beneficial for achieving high-fidelity multispin operations. Our results constitute an important step in comparing the utility of different defect systems by allowing memory controllability to be included systematically in such comparisons.

The paper is organized as follows. In Sec. II, we review the case of a defect spin coupled to a single nuclear spin and driven by π-pulse sequences. In Sec. III, we generalize this to the case of multiple nuclear spins. We first discuss the metric we use to quantify entanglement, and we then apply this to selectively entangle a subset of nuclei in the case of a defect in SiC coupled to ^{13}C and ^{29}Si nuclei. In Sec. IV, we study the dependence of the gate fidelity on the size of the multipartite entangled state, the size of the bath, and the type of control sequence used. We summarize our conclusions in Sec. V.

II. SINGLE NUCLEAR SPIN COUPLED TO DEFECT AND DYNAMICAL DECOUPLING

Taminiau *et al.* [22] demonstrated that, by selecting the pulse intervals of a DD sequence to satisfy a specific resonance condition dictated by the hyperfine (HF) couplings, it is possible to rotate a desired nuclear spin conditionally on the electronic spin state. This is possible because DD sequences can dynamically modify the effective electron-nuclear HF interaction, enabling the coupling of a specific nuclear spin to the electron spin while decoupling others. Well-known examples of DD sequences that are widely used in the quantum information science community include the Carr-Purcell-Meiboom-Gill (CPMG) [30–32] and Uhrig (UDD) [33] sequences. In this section, we review existing results for single nuclear-spin control via electronic spin driving.

As a first step, we review how one can create electron–nuclear-spin entanglement using repeated DD pulse sequences. For instance, one can use the CPMG sequence on the electron and repeat the basic unit N times, i.e., $(\tau/4–\pi–\tau/2–\pi–\tau/4)^N$, where τ is the duration of the unit, and π represents the application of an instantaneous π pulse. These π pulses are implemented experimentally via a microwave drive to induce transitions between electronic spin states directly. In practice, the π pulses have a finite duration and amplitude, and they can be generated using a vector source [34], where their features such as frequency, duration, and amplitude are preset by an arbitrary waveform generator, while their pulse shapes can be Hermite envelopes [24,35].

The Hamiltonian for a single electronic spin in SiC interacting with a single nuclear spin ($I = 1/2$) is given by [36]

$$H = \frac{\omega_L}{2} \, \mathbb{1} \otimes \sigma_z + \frac{A_\parallel}{2} Z_e \otimes \sigma_z + \frac{A_\perp}{2} Z_e \otimes \sigma_x$$
$$= \sigma_{00} \otimes H_0 + \sigma_{11} \otimes H_1. \tag{1}$$

Here ω_L is the Larmor frequency of the nuclear spin; σ_i, with $i \in \{x, y, z\}$, are the Pauli matrices; and $A_\parallel$ ($A_\perp$) is the parallel (perpendicular) component of the HF interaction. The electronic spin operator Z_e is defined as $Z_e = s_0 \sigma_{00} + s_1 \sigma_{11}$, where $\sigma_{jj} = |j\rangle \langle j|$ are the electronic spin projection operators, with $|j = 0\rangle$ and $|j = 1\rangle$ being the two levels of the electronic spin multiplet used to define the two-dimensional qubit space, while s_j is the corresponding spin projection quantum number. For instance, N-V centers in diamond have total spin $S = 1$ and the logical qubit states are $|s_0 = 0\rangle$ and $|s_1 = -1\rangle$ [2]; while the negatively charged silicon vacancy in SiC has $S = 3/2$ and the qubit states are typically defined to be $|s_0 = 1/2\rangle$ and $|s_1 = 3/2\rangle$ [9], or $|s_0 = -1/2\rangle$ and $|s_1 = -3/2\rangle$ [10]. Moreover, $H_j = \frac{1}{2}[(\omega_L + s_j A_\parallel)\sigma_z + s_j A_\perp \sigma_x]$ is the Hamiltonian experienced by the nuclei, which is conditional on the state of the electronic spin.

Notice that Eq. (1) assumes an external magnetic field along the principal axis where the electron Zeeman splitting between the electron and nuclear spins is large. This significant mismatch ensures that σ_z remains a good quantum number throughout the dynamics. This approximation is known as a *secular approximation*. Using the above Hamiltonian, one can show that the evolution operator, after one unit of the pulse sequence, can be written as [22,29]

$$U = \sigma_{00} \otimes R_{\mathbf{n}_0}(\phi_0) + \sigma_{11} \otimes R_{\mathbf{n}_1}(\phi_1), \tag{2}$$

where $R_{\mathbf{n}_j}(\phi_j) = e^{-i\phi_j/2\boldsymbol{\sigma} \cdot \mathbf{n}_j}$ are the two conditional nuclear-spin evolution operators defined by two rotation axes $\mathbf{n}_j$ and two angles ϕ_j. Both $\mathbf{n}_j$ and ϕ_j depend on the electronic spin state and the chosen pulse sequence. The potential of creating controlled gates with the electron as the control qubit and the nuclei as the target qubits is already evident in Eq. (2). For instance, in the case where $\phi_1 = \phi_0 = \pi/2$ and $\mathbf{n}_0 = -\mathbf{n}_1 = \mathbf{x}$, the evolution operator yields (the cross-resonance) $U = \mathrm{CR}_x(\pi/2) = \sigma_{00} \otimes R_\mathbf{x}(\pi/2) + \sigma_{11} \otimes R_\mathbf{{-x}}(\pi/2)$, which is equivalent to the controlled NOT (CNOT) up to local rotations.

To leverage this conditional Hamiltonian to create electron-nuclear entanglement, the electron spin must be prepared in a superposition state, e.g., $|+\rangle = (|0\rangle + |1\rangle)/\sqrt{2}$, while the nuclear spin can be initialized in the state $|0\rangle$. In certain cases, the subsequent application of N DD sequence units makes the two nuclear rotation

operators, $R_{\mathbf{n}_j}(N\phi_j)$, differ. This can happen, for example, if the unit time, τ, is chosen such that the nuclear rotation axes are antiparallel, i.e., $\mathbf{n}_0 \cdot \mathbf{n}_1 = -1$. At this time, the probability, P_+, that the initial state $|+\rangle$ of the electron is preserved reaches the minimum value, signifying the creation of an electron–nuclear-spin Bell pair. This probability (or coherence function) is calculated as $P_+ = (1 + M)/2$, with $M = \frac{1}{2} \mathrm{Re} \, \mathrm{tr}[R_{\mathbf{n}_0}(N\phi_0)R_{\mathbf{n}_1}^\dagger(N\phi_1)]$ [22,29]. For instance, in the case of CPMG pulses, it holds that $\phi_0 = \phi_1 = \phi$ and $M = 1 - \sin^2(N\phi/2)(1 - \mathbf{n}_0 \cdot \mathbf{n}_1)$, where N is the number of applied unit sequences.

This last expression reveals that, for antiparallel axes and accumulated phase $N\phi = \pi/2$, the resulting conditional rotation leads to a dip in the electron's coherence function down to the value $P_+ = 1/2$. The resonance times at which this entanglement occurs can be calculated using the explicit formulas for the nuclear operators $R_{\mathbf{n}_j}(\phi_j)$, setting $\mathbf{n}_0 \cdot \mathbf{n}_1 = -1$, and solving $\mathrm{tr}(R_{\mathbf{n}_0} R_{\mathbf{n}_1}^\dagger)/2 = \cos(\phi_0)\cos(\phi_1) + \mathbf{n}_0 \cdot \mathbf{n}_1 \sin(\phi_0)\sin(\phi_1)$ for time τ, where $R_{\mathbf{n}_j}$ and ϕ_j depend on the pulse sequence and the unit time τ. One can show that for CPMG, UDD$_3$, and UDD$_4$ sequences, the resonance times are given by [22,29]

$$\tau_k \simeq \frac{4\pi(2k - 1)}{\omega_0 + \omega_1}, \tag{3}$$

where $\omega_j = \sqrt{(\omega_L + s_j A_\parallel)^2 + (s_j A_\perp)^2}$, and $k \in \mathbb{Z}^+$ is the resonance order. As reported in [37], the UDD$_4$ sequence has additional resonance times located at $\tau_k \simeq 8\pi(2k - 1)/\tilde{\omega}$; see Fig. 1(d). These expressions for τ_k are approximate and valid for $\omega_L \gg A_\parallel, A_\perp$.

In general, when the resonance condition is satisfied ($\mathbf{n}_0 \cdot \mathbf{n}_1 = -1$), a single DD unit creates a small angle of rotation, as shown in Figs. 1(b)–1(d), and thus a small amount of entanglement. A larger amount of electron–nuclear-spin entanglement can be achieved by iterating the unit sequence N times to accumulate the desired angle of rotation $N\phi_j$. In Fig. 1, we present the angle of rotation versus the unit time for the CPMG, UDD$_3$, and UDD$_4$ sequences. Sequences with an odd number of pulses in the basic unit need to be repeated twice to ensure the electron experiences an even number of π pulses and returns to its initial state [29]. In the case of CPMG and UDD$_3$, the rotation angles are the same, i.e., $\phi_0 = \phi_1$. A straightforward way to create a large amount of entanglement is to set the unit time equal to a resonance time ($\tau = \tau_k$), so that the dot product is always $\mathbf{n}_0 \cdot \mathbf{n}_1 = -1$, and apply N sequences such that the accumulated angle is $N\phi \simeq \pi/2$. This combination leads to a perfect entangling gate $\mathrm{CR}_x(\pi/2)$, which is equivalent to CNOT up to single qubit rotations.

Although the time intervals between the π pulses are given by the same formula for all UUD$_n$ sequences (see Appendix A), the rotation angles are not equal for some of them. The UDD$_4$ sequence leads to a more complicated
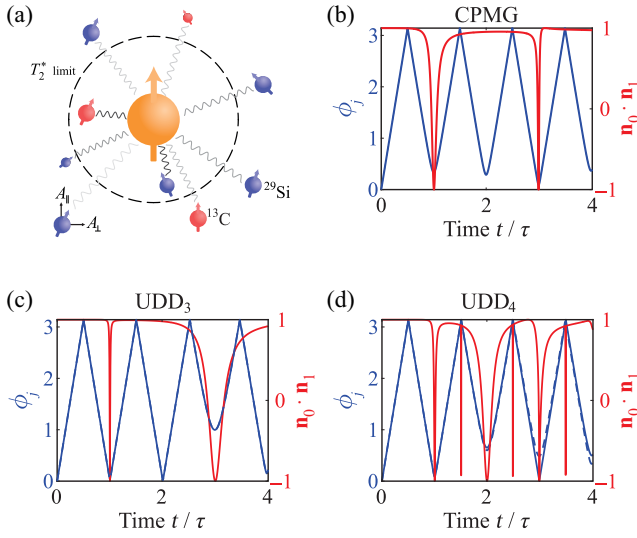
FIG. 1. (a) Schematic depicting a single silicon vacancy coupled to nuclear spins through HF interaction. The spheres denote both nuclear (^{13}C, ^{29}Si) and electronic spins. Additionally, we illustrate the transition distance between the strongly coupled and weakly coupled regimes, depicted as the T_2^* limit (black dashed line). (b)–(d) The rotation angles ϕ_j (solid and dashed blue lines) and the dot product $\mathbf{n}_0 \cdot \mathbf{n}_1$ (red) of nuclear axes plotted as a function of the unit time τ_k of CPMG, UDD$_3$, and UDD$_4$, respectively. For CPMG and UDD$_3$, it holds that $\phi_0 = \phi_1$ and thus the blue lines (solid and dashed) are on top of each other, while in UDD$_4$ the two angles are distinguishable. For the nuclear spin, we set $(\omega_L, A_\parallel, A_\perp) = 2\pi \times (100, 100, 80)$ kHz, and the electron's spin projections are $(s_0, s_1) = (1/2, 3/2)$. The time is normalized to the first-order resonance times $(\tau_{\text{CPMG}}, \tau_{\text{UDD}_3}, \tau_{\text{UDD}_4}) = (4.6487, 4.6444, 4.6495)\ \mu\text{s}$.

evolution of the nuclear spin in which the rotation angle depends differently on the state of the electron. This in turn leads to a nontrivial dependence of the dot product of its rotation axes on N. Thus, even if one fixes a resonance time for the basic UDD$_4$ unit, the nuclear rotation axes can switch from antiparallel to parallel for values of N where ϕ_0 and ϕ_1 become equal [29]. In this case, with parallel axes ($\mathbf{n}_0 \cdot \mathbf{n}_1 = 1$) and equal angles of rotation, the nuclear spin undergoes an unconditional rotation and, thus, no entanglement can be created.

As we show later on, perfect entanglement can also be achieved by easing the restriction of the unit time being equal to a resonance time, as long as the dot product remains negative, $\mathbf{n}_0 \cdot \mathbf{n}_1 < 0$. This is indeed very important since it makes it possible to entangle the electron with several nuclear spins (with different HF interactions) simply by tuning the pulse spacing τ to such a "multinuclear resonance" time. Furthermore, the above feature can be combined with the fact that π-pulse sequences can also average out the interactions of the electron with unwanted spins, ensuring some degree of selectivity with a target set of spins.

III. ENTANGLEMENT IN DEFECT–MULTINUCLEAR-SPIN SYSTEMS

We now move on to consider a defect electronic spin coupled to a multinuclear-spin register. We first discuss metrics for gauging the ability of HF interactions and DD sequences to create entanglement in these systems. We then discuss how to apply these metrics to select which nuclear spins to entangle with the electronic spin and which to decouple. We focus on the case of defects in SiC coupled to two nuclear species (^{13}C and ^{29}Si) for concreteness.

A. Quantifying entanglement in electron–multinuclear-spin systems

Before we develop protocols for controlling and entangling multiple nuclear spins, we first have to discuss how we quantify entanglement in multinuclear-spin registers. We begin with considering the entangling power for a defect coupled to a single nuclear spin and then extend the formalism to multiple nuclear spins by employing the concept of one-tangles [38]. As will become clear in Sec. IV, these quantities will guide our design toward selective multinuclear-spin entangling gates.

The entangling power is a general property of logical gate operations that disregards the details of a gate and focuses solely on its entanglement capabilities [39]. The entangling power of a two-qubit operator can be expressed as [40]

$$\epsilon_p = 1 - |G_1|, \tag{4}$$

where the function G_1 is a Makhlin invariant (see Appendix B) whose explicit form in the present context of electron-nuclear entanglement is

$$G_1 = \left(\cos\frac{\phi_0(N)}{2} \cos\frac{\phi_1(N)}{2} + n_{01} \sin\frac{\phi_0(N)}{2} \sin\frac{\phi_1(N)}{2} \right)^2. \tag{5}$$

Here, we use the fact that, for any given π-pulse sequence repeated N times, the electron-nuclear evolution operator maintains the structure described in Eq. (2), with the only difference being that ϕ_j is now replaced by the total rotation angle $\phi_j(N)$.

In Eq. (4), we discarded an overall factor of $2/9$ for convenience, and thus the entangling power takes values in the range $0 \le \epsilon_p \le 1$. It is evident that when G_1 becomes 0, the entangling power is maximized, reaching its peak at $\epsilon_p = 1$ for the two-qubit case. The minima of G_1 occur at $N = (2k+1)\pi/(\phi_0 + \phi_1)$; however, N is an integer and so the value of this expression must be rounded in general. Notice that G_1 can also be zero for other N values, provided that $\mathbf{n}_0 \cdot \mathbf{n}_1 \le 0$. In Fig. 2 we plot the scaled entangling power, ϵ_p, for a single nuclear spin coupled to
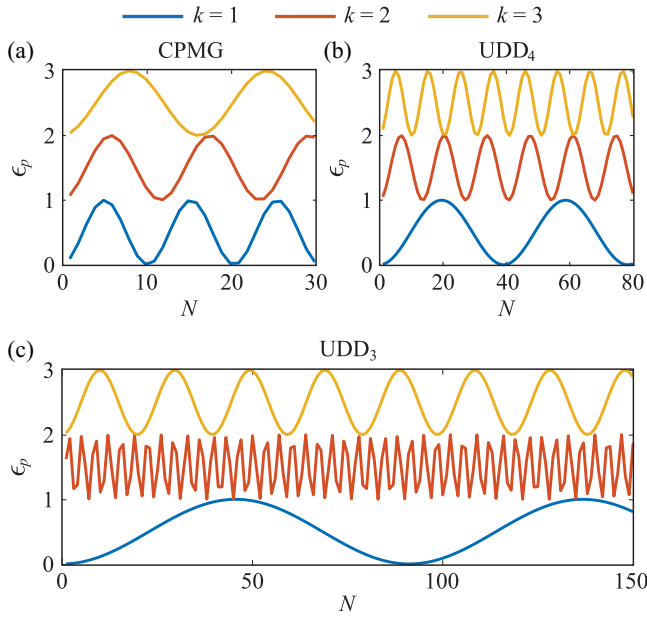
FIG. 2. Scaled entangling power as a function of resonance order ($k = 1$, blue lines; $k = 2$, red lines; $k = 3$, yellow lines) and the number of repetitions N of the CPMG (a), UDD$_4$ (b), and UDD$_3$ (c) units. For the nuclear spin, we set $(\omega_L, A_\parallel, A_\perp) = 2\pi \times (-300, 60, 30)$ kHz, and the electron's spin projections are $(s_0, s_1) = (1/2, 3/2)$. The resonance times are optimized around the analytical resonance time: for CPMG, $(\tau_1, \tau_2, \tau_3) = (4.1378, 12.354, 20.6201)$ µs; for UDD$_3$, $(\tau_1, \tau_2, \tau_3) = (4.1360, 12.404, 20.6170)$ µs; and for UDD$_4$, $(\tau_1, \tau_2, \tau_3) = (4.1393, 12.3743, 20.26451)$ µs. The scaled entangling power takes values $\epsilon_p \in [0, 1]$, and the offsets in the graphs are used for illustration purposes only.

the electron versus the number of iterations and the resonance order k. We see that the frequency of the maxima of ϵ_p depends on the pulse sequence and the resonance order, an expected behavior, since these features directly affect the rotation angle per iteration.

To quantify the distribution of entanglement within the entire system, consisting of one electronic and many nuclear spins, we expand the notion of entangling power beyond two qubits. To that end, we utilize the one-tangles [41] which measure the overall entanglement within a state by assessing all possible bipartitions of the system. By virtually partitioning the total system into subsystems, we quantify the level of correlations between these subsystems (this is also known as bipartition entanglement). We choose this metric to quantify the entanglement of our gate, and for each bipartition we separate only one qubit (either electron or nuclear spin) from the rest of the system. Note that one-tangles exclusively convey information about the system's entanglement capacity, and they cannot differentiate between states belonging to different categories [e.g., W states versus GHZ (Greenberger-Horne-Zeilinger)

states in the n-partite case, $n \geq 3$] [38]. We find one-tangles to be a convenient metric in our system since we are interested in its entanglement capacity, rather than generating specific entangled states.

For the sake of completeness, we note that, for a pure state $|\psi\rangle$, the one-tangle is defined by the generalized concurrence [38]

$$\tau_{g|g'}(|\psi\rangle) := 2(1 - \text{tr}[\rho_{g'}^2]), \quad \rho_{g'} = \text{tr}_g[|\psi\rangle\langle\psi|], \quad (6)$$

where $g|g'$ denotes the bipartition or the splitting of the Hilbert space. Equation (6) bounds one-tangles in the range $[0, \ 2 - 2/\min(d, d')]$, where d (d') is the dimension of partition g (g').

The present form of Eq. (6) is not very effective for measuring the entanglement of multinuclear operations because it relies on the initial state. To address this, we need to consider an average across all initial states. Specifically, we employ the bipartition entangling power, which is the average of the one-tangle across all initial product states. According to Ref. [38], this is calculated by averaging over single-qubit unitaries U_i applied to initial product state $|\psi_0\rangle$, denoted as $|\Psi\rangle := |\psi_0\rangle^{\otimes_i} = U_i^{\otimes_i} |\psi_0\rangle^{\otimes_i}$, resulting in $\epsilon_{g|g'}(U) := \langle \tau_{g|g'}(U|\Psi\rangle) \rangle_{U_i}$. Here, the index i ranges from 1 to n, where n represents the total number of qubit systems. Ordinarily, this "one-tangling power" is difficult to calculate explicitly for a generic many-body Hamiltonian. However, as first shown in Ref. [29], it can be analytically computed for the type of electron–nuclear-central-spin system that we have in defect systems. Although $\epsilon_{g|g'}(U)$ characterizes the bipartite entanglement generated by the unitary U and is not a state-dependent property, for brevity we will still refer to it as a "one-tangle" in what follows.

Before discussing the explicit expression for the one-tangle, we first introduce the Hamiltonian of a single electronic spin coupled to multiple nuclear spins. We neglect the nuclear-nuclear interactions because the electron-to-nuclear dipole moment ratio is about 1836, thus rendering these interactions significantly smaller. Additionally, given the low abundance of nuclear spins, we can assume they are sufficiently spaced apart such that the $1/r_{ij}^3$ term does not compensate for the aforementioned difference in dipole moment magnitudes. The Hamiltonian for L nuclear spins is given by

$$H = \sum_{j=0,1} \sigma_{jj} \otimes \left(H_j^{(1)} \otimes \mathbb{1}_{2^{L-1}} + \mathbb{1} \otimes H_j^{(2)} \otimes \mathbb{1}_{2^{L-2}} + \cdots \right.$$
$$\left. + \mathbb{1}_{2^{l-1}} \otimes H_j^{(l)} \otimes \mathbb{1}_{2^{L-l}} + \cdots + \mathbb{1}_{2^{L-1}} \otimes H_j^{(L)} \right), \quad (7)$$

with

$$H_j^{(l)} = \frac{\omega_L^{(l)} + s_j A_\parallel^{(j)}}{2} \sigma_z^{(l)} + \frac{s_j A_\perp^{(l)}}{2} \sigma_x^{(l)}, \quad (8)$$

where $\sigma_x^{(l)}$ and $\sigma_z^{(l)}$ are the Pauli operators acting only on the lth nuclear spin (the identity operator acts on all the other spins).

Notice that the Larmor frequency, $\omega_L^{(l)}$, is different for different types of nuclear spins. Recall that for ^{13}C the gyromagnetic ratio is $\gamma_{13C} = 2\pi \times 10.7084$ MHz/T, and for ^{29}Si the ratio is $\gamma_{29Si} = -2\pi \times 8.465$ MHz/T. The above secular form of the Hamiltonian makes it apparent that the terms in parentheses commute with each other, i.e., $[\mathbb{1} \otimes H_j^{(k)} \otimes \mathbb{1}, \ \mathbb{1} \otimes H_j^{(l)} \otimes \mathbb{1}] = 0$, where $\mathbb{1}$ has the appropriate dimensions in each position. As a result of this feature, in the case of a single electronic spin coupled to multiple nuclear spins, the π-pulse sequences generate an evolution operator which is a sum of terms, namely

$$U = \sum_{j=0,1} \sigma_{jj} \bigotimes_{l=1}^{L} R_{\mathbf{n}_j}^{(l)}\big(\phi_j^{(l)}(N)\big), \qquad (9)$$

with L denoting the total number of nuclear spins and $\phi_j^{(l)}(N)$ being the total angle of rotation after N iterations.

From now on, we will denote the total angle or rotation simply as $\phi_j^{(l)}$. The last equation reveals that the evolution operator of the total system is defined by the evolution of each nuclear spin conditional on the state of the electron. Each nuclear-spin evolution is independent of the rest, which implies that the entanglement dynamics of the entire system can be decomposed into pairwise electron-nuclear correlations. This feature enables us to derive analytical expressions for the average of the one-tangles across varying numbers of nuclear spins.

In Ref. [29], it was shown that the one-tangle of a single nuclear spin, when partitioned from the remaining electron-nuclear register, is given by

$$\epsilon_{p|q}^{\text{nuclear}} = 1 - G_1^{(q)}, \qquad (10)$$

where we omit the 2/9 overall factor for simplicity, as we did in Eq. (4), and $G_1^{(q)}$ denotes the first Makhlin invariant for the qth nuclear spin. Equation (10) holds for $n \geq 3$ qubits, while for $n = 2$ qubits the average of the one-tangles is the same as the two-qubit entangling power given in Eq. (4).

It is worth noting that the one-tangle of a nuclear spin is affected solely by the factors governing its evolution, owing to the tensor product structure of the overall evolution operator U. Essentially, altering the partitioned nuclear spin within the register modifies Eq. (10) via its $G_1^{(q)}$, indicating a different level of entanglement between the partitioned spin and the remaining electron-nuclear register. Although Eq. (10) aligns with the two-qubit entangling power from Eq. (4) in a disjointed view, the interpretations of these equations differ. More specifically, Eq. (4) tells us to what extent the two-qubit gate, created by

the π-pulse sequences, can generate an electron–nuclear-spin Bell state, while Eq. (10) describes correlations in the multispin register and, therefore, needs to respect the monogamy of entanglement [29].

Before we proceed, we should mention that we use entangling power as a key measure in this work due to its unique advantages over traditional entanglement metrics. Unlike concurrence or Von Neumann entropy, which require calculating and averaging entanglement across multiple input states, entangling power provides a state-independent analysis of a gate's ability to generate entanglement. This makes it especially suitable for our study, where we aim to assess gate performance without being limited to specific initial or output states. In the context of gate design and optimization, where broad applicability and efficiency are crucial, entangling power allows us to quickly evaluate and compare different control sequences. Its robustness and computational efficiency make it ideal for examining the performance of quantum operations in systems with large, weakly coupled nuclear-spin registers. By utilizing entangling power, we ensure that our analysis captures general performance trends across different configurations and control sequences, providing a broader and more reliable evaluation of gate fidelities

B. Multiple nuclear spins: Single-shot entanglement

In this subsection, we exploit the twofold feature of DD sequences by entangling the electron selectively to a set of nuclear-spin target(s) in a nuclear-spin bath. In detail, we use DD sequences to couple the electron to a specific set while, simultaneously, decoupling it from the rest of the bath. We quantify the amount of target and unwanted entanglement using the one-tangles mentioned in Sec. III A. This approach of synchronous maximization of multiple one-tangles was first proposed in Ref. [29]. In the following example and for all subsequent simulations, we will consider only ideal, error-free DD sequences. For information regarding amplitude errors in the pulse sequences, see Appendix C.

To illustrate the method, we consider a single defect and a total of three nuclear spins, ^{13}C and ^{29}Si. Each nuclear spin is characterized by its HF interaction parameters, and thus by its resonance times, approximated in Eq. (3). There are two key parameters that we need to determine: the duration τ of one sequence unit and the number of iterations N. Our goal is to choose the unit time τ and the number of iterations N such that we entangle a desired number of nuclear spins to the electron; in the example that follows, this can be one, two, or three. For simplicity, we present the algorithm only for CPMG, but all the steps remain the same for UDD sequences too.

As a first step, we calculate the resonance times $\tau_k^{(l)}$ for every nuclear spin, $l \in \{1, 2, 3\}$. To do so, we use Eq. (3) to reach the vicinity of the resonance, and then we find

the precise value of $\tau_k^{(l)}$ numerically since we know that at this value the dot product of the axes of rotation, for the respective spins, is equal to -1, i.e., $\mathbf{n}_0 \cdot \mathbf{n}_1 = -1$. As mentioned above, perfect entanglement can be achieved as long as $\mathbf{n}_0 \cdot \mathbf{n}_1 \leq 0$, so we allow the unit time to take values around the resonance times, $\tau \in [\tau_k^{(l)} - \delta\tau, \ \tau_k^{(l)} + \delta\tau]$. Next, we find the one-tangle, $\epsilon_p^{(l)}(\tau, N)$, for every nuclear spin from Eq. (10), which is a function of the unit time τ chosen in the above intervals, and the number of repetitions N. We also set a maximum gate time T_g so that $N\tau \leq T_g$. All the information we need to choose τ and N is given by $\epsilon_p^{(l)}(\tau, N)$. For instance, if we want to entangle all three spins with the electron we must choose a pair of (τ, N) such that $\epsilon_p^{(l)}$ is above a threshold ϵ_p^{th} and close to unity for $l = 1, 2, 3$. Another case would be to create a register of two nuclear spins, known as target spins, and decouple the register from the third nuclear spin. This can be achieved by choosing a pair of (τ, N) such that two one-tangle values, $\epsilon_p^{(l)}(\tau, N)$, are maximized and larger than ϵ_p^{th} while the third one is minimized and smaller than ϵ_p^{th}. A pseudocode of the above recipe can be found in Appendix D.

To make the above example more concrete, we present a numerical application of the proposed recipe. In Fig. 3 we show that, for a silicon vacancy, with quantum numbers $(s_0, s_1) = (1/2, 3/2)$, and three nuclear spins (one ^{13}C, two ^{29}Si), we can selectively entangle nuclear spins with the electron, or decouple them from it, simply by using different combinations of (τ, N). Figure 3(a) shows that a register of three spins and the electron can be created by setting $(\tau, N) = (26.54\,\mu s, 28)$ for a CPMG sequence, while the size of the register is reduced to two nuclear spins in Fig. 3(b) by choosing $(\tau, N) = (79.298\,\mu s, 20)$, and to one nuclear spin in Fig. 3(c) for $(\tau, N) = (22.268\,\mu s, 12)$. Note that, in Fig. 3(a), we simultaneously optimize all three one-tangles, while in the other two panels, we minimize the unwanted one-tangles but do not attempt to maximize the wanted ones. This combination of features, being able to change the size of the register while effectively reducing the crosstalk from the bath, is essential for creating a quantum register. Moreover, the total gate time needed is always shorter than the nuclear spin coherence time T_2^*, which ranges from 3 to 17 ms [34]. Also, the reduction of the crosstalk is of significant importance because, as we will show in the next section, it affects the gate fidelity. In the next section, we extend the algorithm by including more DD sequences and a range of register sizes and bath qubit assignments.

IV. FIDELITY DEPENDENCE ON REGISTER AND BATH SIZE

In this section, we quantify the effect of the register size and the spin bath on the gate fidelity in the case of silicon monovacancies and divacancies coupled to a nuclear bath of ^{13}C and ^{29}Si nuclear spins. We begin by
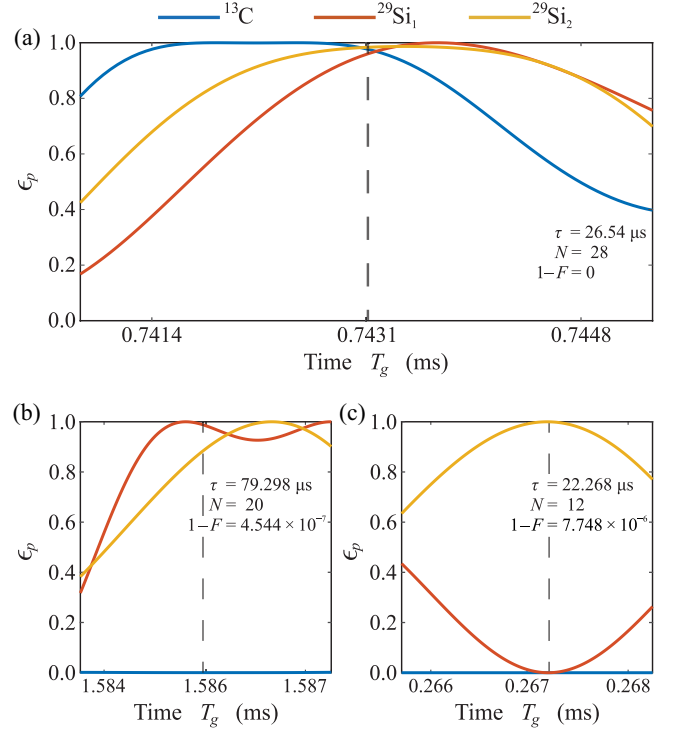

FIG. 3. Scaled one-tangles for three nuclear spins coupled to the electron. We present numerical results for the algorithm proposed in the main text using CPMG sequences for a set of (a) three spins, (b) two spins, and (c) one spin coupled to the electronic spin. Each graph depicts the entangling power between a single nuclear spin partitioned from the rest of the system as a function of $N\tau$, where τ is the unit time and N the number of iterations. The horizontal axis in each panel corresponds to fixing N to its optimal value and scanning τ. The optimal values of τ and N in each case are given in the graphs, while the vertical dashed line indicates the corresponding gate time $N\tau$ at the optimal point. The entangling power of the nuclear spins $(\epsilon_p^{\text{C}}, \epsilon_p^{\text{Si}_1}, \epsilon_p^{\text{Si}_2})$ in each case are (a) $(0.9766, 0.96, 0.9837)$, (b) $(2.047 \times 10^{-6}, 0.9879, 0.8838)$, and (c) $(8.4 \times 10^{-6}, 2.3 \times 10^{-5}, 0.9999)$. The Larmor frequencies are $(\omega_L^{\text{C}}, \omega_L^{\text{Si}}) = 2\pi \times (88.8797, -70.2595)$ kHz, while the HF couplings are $(A_\parallel^{\text{C}}, A_\perp^{\text{C}}) = 2\pi \times (151.3741, 105.0043)$ kHz, $(A_\parallel^{\text{Si}_1}, A_\perp^{\text{Si}_1}) = 2\pi \times (96.2445, 180.9921)$ kHz, and $(A_\parallel^{\text{Si}_2}, A_\perp^{\text{Si}_2}) = 2\pi \times (122.1684, 123.7244)$ kHz. The HF values for the ^{13}C and the ^{29}Si are drawn from uniform distributions in the intervals $[10, 200]$ kHz and $[0.5, 200]$ kHz, respectively.

introducing a way to optimize the gate fidelity. We then implement this method for a monovacancy coupled to multiple nuclear spins, and, finally, we examine the case of a mixed bath where the nuclear spins have the same sign in gyromagnetic ratio.

A. Fidelity optimization

Let us consider a scenario with a total of L nuclear spins, where K of them are the target nuclei exhibiting maximal

one-tangles. The unwanted nuclei, $L - K$, impact the target gate because they generally possess some residual level of entanglement with the electron. Consequently, truncating the evolution operator to the target subspace results in a nonunitary operation. Takou *et al.* [29] demonstrated how to circumvent this issue using the Kraus operator representation of the partial trace channel. This approach allows us to directly manipulate the total evolution operator without specifying an initial state for the system. We use the analytical expression for the gate fidelity within the target subspace by employing the operator-sum representation [29]. As the target gate we consider the evolution operator

$$U_0 = \sum_{j=0,1} \sigma_{jj} \bigotimes_{k=1}^{K} R_{\mathbf{n}_j^{(k)}}\big(\phi_j^{(k)}\big), \qquad (11)$$

that we design in the ideal case of no unwanted spins. This target gate is ignorant of the presence of unwanted spins, i.e., it is defined in the truncated space of the electron and the K target nuclear spins. The total evolution operator, given in Eq. (9), can be rewritten as

$$U = \sum_{j=0,1} \sigma_{jj} \bigotimes_{k=1}^{K} R_{\mathbf{n}_j^{(k)}}\big(\phi_j^{(k)}\big) \bigotimes_{l=1}^{L-K} R_{\mathbf{n}_j^{(K+l)}}\big(\phi_j^{(K+l)}\big), \quad (12)$$

where, for convenience, we permuted the spins such that the register spins appear first in the tensor product with the electron spin projector and the unwanted spins appear in the last positions.

In the context of the operator-sum representation [42], the fidelity of a quantum operator has the form

$$F = \frac{1}{d(d+1)} \sum_j \mathrm{tr}[(U_0^\dagger E_j)^\dagger U_0^\dagger E_j] + |\mathrm{tr}[U_0^\dagger E_j]|^2, \quad (13)$$

where $d = 2^{K+1}$ represents the dimension of the target subspace, which includes the electron and K target spins. The index j iterates through the environment's 2^{L-K} complete computational basis states; the Kraus operators E_j describe the quantum channel denoted by $\mathcal{E}(\rho) = \sum_j E_j \rho E_j^\dagger$ and they satisfy the completeness relation $\sum_j E_j^\dagger E_j = 1$. The Kraus operators are given by [29]

$$E_i = \sum_j c_j^{(i)} p_j^{(i)} \sigma_{jj} \bigotimes_{k=1}^{K} R_{\mathbf{n}_j^{(k)}}\big(\phi_j^{(k)}\big), \qquad (14)$$

where

$$c_j^{(i)} \equiv \prod_{m=m_1}^{m_M} [\cos(\phi_j^{(m)}/2) - i n_{z,j}^{(m)} \sin(\phi_j^{(m)}/2)]$$

and

$$p_j^{(i)} \equiv \prod_{\xi=\xi_1}^{\xi_{L-K-M}} [-(i n_{x,j}^{(\xi)} + i n_{y,j}^{(\xi)}) \sin(\phi_j^{(\xi)}/2)],$$

while $\{n_x, n_y, n_z\}$ correspond to the rotation axis components of each nuclear spin. Also, M counts the number of the environment spins in the $|0\rangle$ state, while the other $K - L - M$ are in the $|1\rangle$ state. In the case where $M = 0$, so that all the unwanted spins are in the $|1\rangle$ state, it holds that $c_j^{(i)} = 1$, and when $M = L - K$, all the unwanted spins are in the $|0\rangle$ state, in which case $p_j^{(i)} = 1$.

Substituting Eqs. (11) and (14) into Eq. (13), the gate fidelity becomes

$$F = \frac{1}{2^{K+1} + 1}\left(1 + 2^{K-1} \sum_k \left|\sum_{j=0,1} c_j^{(k)} p_j^{(k)}\right|^2\right). \quad (15)$$

Obviously, in the absence of unwanted nuclear spins, the fidelity is unity. The data in Fig. 3 reveal the direct connection between the one-tangles and the fidelity of the target gate. We also find that the fidelity of the target gate is mostly affected by the largest one-tangle of the unwanted spins, which agrees with Ref. [29]. This last observation is especially important since it identifies the parameter we should minimize in order to maximize the target gate's fidelity.

As mentioned in Ref. [29], the gate error can exhibit sudden spikes that reach significantly high levels even at low one-tangle values. This behavior arises because the presence of unwanted spins can disrupt the expected ideal evolution of the isolated target system described by Eq. (11). However, despite this deviation, the resulting gate operation might exhibit a greater overlap with other entangling gate operations that are equivalent to Eq. (11) up to local gates. To account for this, we can generalize the target gate to include an arbitrary single-qubit rotation on the electronic spin, $R_{\mathbf{n}^e}(\theta)$, and then optimize over the axis $\mathbf{n}^e$ and angle θ of the rotation. The target gate thus becomes, $\tilde{U}_0 = R_{\mathbf{n}^e}(\theta) U_0$, leading to the fidelity (see Appendix E for the proof)

$$F_{\mathrm{opt}} = \frac{1}{2^{K+1} + 1}\left(1 + 2^{K-1} \sum_k \left|\sum_{j=0,1} c_j^{(k)} p_j^{(k)} \{\cos(\theta/2)\right.\right.$$
$$\left.\left. + i(-1)^j \sin(\theta/2) n_z^e\}\right|^2\right). \tag{16}$$

In principle, we can optimize the above relation over the range $\theta \in [0, 2\pi)$ for the rotation angle, and $n_z^e \in [-1, 1]$ for the z component of the rotation axis. However, the maximum fidelity can be achieved only when $|n_z^e| = 1$.
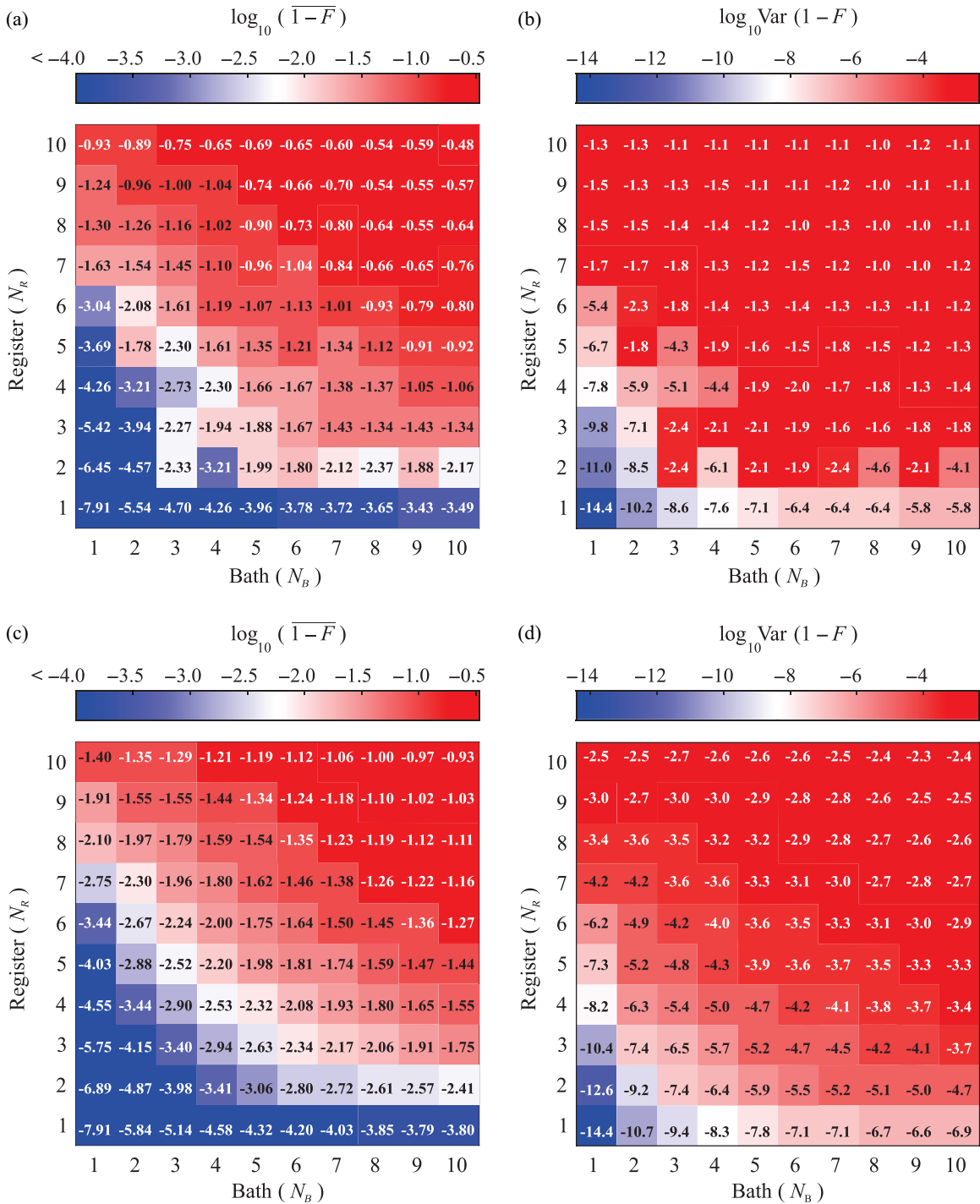
FIG. 4. Gate infidelity $(1-F)$ versus the size of the bath (unwanted spins) and the size of the register (wanted or target spins) before (a),(b) and after (c),(d) optimization over single-qubit rotations on the electronic spin. In panels (a) and (c) we plot the decimal logarithm of the statistical average of infidelity, i.e., $\log_{10}(\overline{1-F})$, while in panels (b) and (d) we plot the variance of the infidelity on the same logarithmic scale $\log_{10}\text{Var}(1-F)$. The numbers in each tile give the value of $\log_{10}(\overline{1-F})$ in panels (a) and (c), and $\log_{10}\text{Var}(1-F)$ in panels (b) and (d). In the above simulations, we considered SiC samples with a silicon monovacancy with total spin $S=3/2$, and the electron qubit is defined by $(s_0, s_1) = (1/2, 3/2)$. The HF values for the ^{13}C and the ^{29}Si were drawn from uniform distributions in the intervals $2\pi \times [10, 200]$ kHz and $2\pi \times [0.5, 200]$ kHz, respectively. The entangling power threshold was set to $\epsilon_p^{\text{th}} = 0.85$; the magnetic field is $B = 83$ G, leading to Larmor frequencies $(\omega_L^C, \omega_L^{Si}) = 2\pi \times (88.8797, -70.2595)$ kHz; and the relative abundance was kept constant for all the cases, i.e., ^{29}Si:^{13}C $= 4.7\%$:$1.1\% = 4.27$. Every data point on the heat maps was obtained from 200 realizations, and for each trajectory we kept the combination (τ, N) that resulted in the lowest maximum unwanted one-tangle.

TABLE I. Fitting parameters for the fit function $\log_{10}(\overline{1 - F_{N_R}}) = a_{N_R} e^{b_{N_R} N_B} + c_{N_R} e^{d_{N_R} N_B}$.

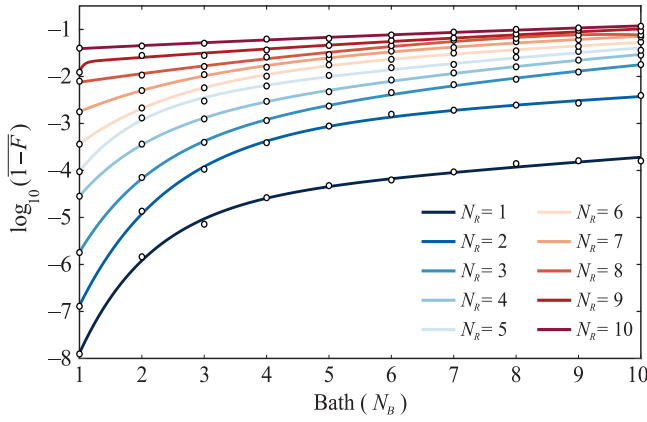| N_R	a	b	c	d
1	−7.594	−0.876	−4.857	−0.026
2	−7.384	−0.712	−3.365	−0.032
3	−5.372	−0.833	−3.665	−0.073
4	−3.556	−0.873	−3.306	−0.076
5	−4.041	−1.075	−2.835	−0.071
6	−2.577	−0.641	−2.196	−0.054
7	−1.530	−0.476	−1.895	−0.051
8	−2.322	−0.089	$−8.5 \times 10^{-5}$	0.758
9	$−3.4 \times 10^6$	−16.56	−1.798	−0.059
10	−1.476	−0.046	0	0

FIG. 5. Statistical average of the infidelity (circles) and fits (solid lines) versus the spin-bath size. The lines are fits of the function $\log_{10}(\overline{1 - F_{N_R}}) = a_{N_R} e^{b_{N_R} N_B} + c_{N_R} e^{d_{N_R} N_B}$ to the collected data (circles). Each line refers to a different register size N_R, and the respective fitting parameters a, b, c, and d are given in Table I.

This can be understood by simply noticing that the fidelity in Eq. (16) is maximized when the second term in the parentheses becomes $2^{K-1} \times 2^2$, and this cannot happen when the factors in the summation are multiplied with a complex number which has norm smaller than unity. In light of this, the rotation axis must be set to $\mathbf{n}^e = \mathbf{z}$, and then we can optimize over the rotation angle $\theta \in [0, 4\pi)$.

B. Average fidelity as a function of register and bath size

In the following simulations, we presume an electron spin with $S = 3/2$ with the qubit defined using the $(s_0, s_1) = (1/2, 3/2)$ spin states, which correspond to a silicon monovacancy defect in SiC [8–10]. The nuclear Larmor frequencies are specified as $(\omega_L^C, \omega_L^{Si}) = 2\pi \times (88.8797, -70.2595)$ kHz for ^{13}C and ^{29}Si nuclei, respectively. Because of the absence of experimental data on weakly coupled spins in SiC and the fact that their HF values are less dependent on the exact lattice positions, we draw the HF values from uniform distributions in the ranges $2\pi \times [10, 200]$ kHz and $2\pi \times [0.5, 200]$ kHz for ^{13}C and ^{29}Si nuclei, respectively. These nuclei are weakly coupled since the HF parameters are smaller than $1/T_2^*$, which is typically a few hundred kilohertz for N-V centers [43,44] or, in general, when $A_\parallel, A_\perp \ll 1$ MHz [45] (approximately 1 MHz is also the electron linewidth for the neutral divacancy in SiC [11]).

Because of the low natural abundance of nuclear spins, strongly interacting spins are rare and can be easily decoupled since their resonance times are very far from those of weakly coupled spins. As a result, their inclusion would not impact the results presented here. Moreover, to ensure the distinctness of spins chosen through random generation, we impose a condition on the discrepancy of HF values; we stipulate that at least one HF value ($A_\parallel$ or $A_\perp$) should deviate by at least $2\pi \times 10$ kHz from the others. This condition is chosen to ensure the generation of sufficient nuclei within the HF range with distinct HF values in order to simulate a realistic silicon vacancy in a SiC sample. Our goal is to examine the dependence of the fidelity on several register-bath size combinations. To do so, we use the algorithm described in Sec. III B, aiming to maximize the one-tangles of the target spins while minimizing those of the unwanted spins. Contrary to the simple example shown in Fig. 3, now we will explore the capabilities of five resonances ($k \in \{1, 2, 3, 4, 5\}$) of the CPMG, UDD$_3$, and UDD$_4$ pulse sequences.

In Fig. 4, we show results from 200 realizations for the case where we have a silicon vacancy defect coupled to $N_R + N_B$ total nuclear spins, where N_R and N_B are the number of nuclear spins in the register and the bath, respectively. In Fig. 4(a),(c) we present the statistical average of the infidelity, $1 - F$, and in Fig. 4(b),(d) its variance, $\text{Var}(1 - F)$, both on a logarithmic scale. For instance, a square data point depicts the statistical average (or variance) of infidelity for a register size N_R and bath size N_B over 200 realizations. The heat maps in Fig. 4(a),(b) show the fidelity and the variance obtained from Eq. (15), while those in Fig. 4(c),(d) show the same quantities after the optimization over single-qubit rotations on the electron spin; see Eq. (16). Comparing the two rows, one can see that in most cases both the infidelity and its variance become smaller, meaning that the optimization leads to an increase in average fidelity, and the fidelities are concentrated around the average. The highest gain occurred for $(N_B, N_R) = (3, 2)$ where the infidelity dropped by 1.6 orders of magnitude, while the variance dropped by five orders of magnitude.

Now let us focus on the lower set of heat maps. As expected, in Fig. 4(c), the best fidelity is obtained in the case of a single target and a single unwanted spin. Also, for small register size, $N_R \leq 5$, there is an exponential decrease in fidelity as the bath size N_B increases. Moreover, Fig. 4(c) reveals a clear deterioration of fidelity not
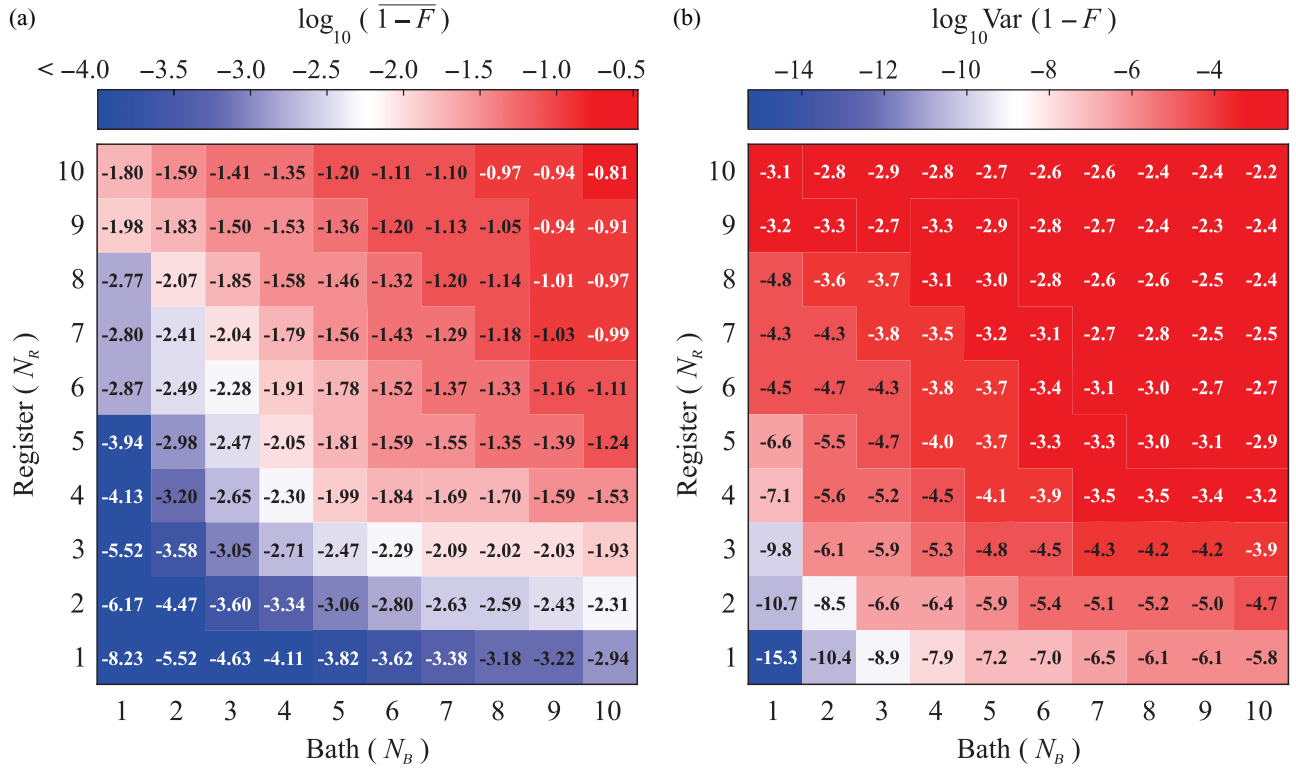
(a) $\log_{10}(\overline{1-F})$

< -4.0	-3.5	-3.0	-2.5	-2.0	-1.5	-1.0	-0.5

Register (N_R)	1	2	3	4	5	6	7	8	9	10
10	-1.80	-1.59	-1.41	-1.35	-1.20	-1.11	-1.10	-0.97	-0.94	-0.81
9	-1.98	-1.83	-1.50	-1.53	-1.36	-1.20	-1.13	-1.05	-0.94	-0.91
8	-2.77	-2.07	-1.85	-1.58	-1.46	-1.32	-1.20	-1.14	-1.01	-0.97
7	-2.80	-2.41	-2.04	-1.79	-1.56	-1.43	-1.29	-1.18	-1.03	-0.99
6	-2.87	-2.49	-2.28	-1.91	-1.78	-1.52	-1.37	-1.33	-1.16	-1.11
5	-3.94	-2.98	-2.47	-2.05	-1.81	-1.59	-1.55	-1.35	-1.39	-1.24
4	-4.13	-3.20	-2.65	-2.30	-1.99	-1.84	-1.69	-1.70	-1.59	-1.53
3	-5.52	-3.58	-3.05	-2.71	-2.47	-2.29	-2.09	-2.02	-2.03	-1.93
2	-6.17	-4.47	-3.60	-3.34	-3.06	-2.80	-2.63	-2.59	-2.43	-2.31
1	-8.23	-5.52	-4.63	-4.11	-3.82	-3.62	-3.38	-3.18	-3.22	-2.94

Bath (N_B): 1 2 3 4 5 6 7 8 9 10

(b) $\log_{10}\text{Var}(1-F)$

-14	-12	-10	-8	-6	-4

Register (N_R)	1	2	3	4	5	6	7	8	9	10
10	-3.1	-2.8	-2.9	-2.8	-2.7	-2.6	-2.6	-2.4	-2.4	-2.2
9	-3.2	-3.3	-2.7	-3.3	-2.9	-2.8	-2.7	-2.4	-2.3	-2.4
8	-4.8	-3.6	-3.7	-3.1	-3.0	-2.8	-2.6	-2.6	-2.5	-2.4
7	-4.3	-4.3	-3.8	-3.5	-3.2	-3.1	-2.7	-2.8	-2.5	-2.5
6	-4.5	-4.7	-4.3	-3.8	-3.7	-3.4	-3.1	-3.0	-2.7	-2.7
5	-6.6	-5.5	-4.7	-4.0	-3.7	-3.3	-3.3	-3.0	-3.1	-2.9
4	-7.1	-5.6	-5.2	-4.5	-4.1	-3.9	-3.5	-3.5	-3.4	-3.2
3	-9.8	-6.1	-5.9	-5.3	-4.8	-4.5	-4.3	-4.2	-4.2	-3.9
2	-10.7	-8.5	-6.6	-6.4	-5.9	-5.4	-5.1	-5.2	-5.0	-4.7
1	-15.3	-10.4	-8.9	-7.9	-7.2	-7.0	-6.5	-6.1	-6.1	-5.8

Bath (N_B): 1 2 3 4 5 6 7 8 9 10

FIG. 6. Gate infidelity $(1-F)$ versus the size of the bath (unwanted spins) and the size of the register (wanted or target spins) upon optimization over single-qubit rotations on the electronic spin. (a) Plot of the decimal logarithm of the statistical average of infidelity, i.e., $\log_{10}(\overline{1-F})$; (b) plot of the variance of the infidelity on the same logarithmic scale $\log_{10}\text{Var}(1-F)$. The numbers in each tile give the value of $\log_{10}(\overline{1-F})$ and $\log_{10}\text{Var}(1-F)$, respectively. In the above simulations, we considered SiC samples with a silicon divacancy with total spin $S=1$, and the electron qubit is defined by $(s_0,s_1)=(0,-1)$. The HF values for the ^{13}C and ^{29}Si nuclei were drawn from uniform distributions in the intervals $2\pi \times [10,200]$ kHz and $2\pi \times [0.5,200]$ kHz, respectively. The entangling power threshold was set to $\epsilon_p^{\text{th}}=0.85$; the magnetic field is $B=584$ G, leading to Larmor frequencies $(\omega_L^C,\omega_L^{\text{Si}})=2\pi \times (625.37,-494.35)$ kHz; and the relative abundance was kept constant for all the cases, i.e., ^{29}Si:^{13}C = 4.7%:1.1% = 4.27. Every data point on the heat maps was obtained from 100 realizations, and for each trajectory we kept the combination (τ,N) that resulted in the lowest maximum unwanted one-tangle.

only with the bath size but also with the register size. This can be explained by considering that the generation of entanglement links between the electron and the register spins, while simultaneously decoupling unwanted spins using DD pulses, becomes very challenging when the register size gets larger. The same happens with the variance, where we see that it grows with the total number of spins, leading to an increasing spread in the fidelity distribution, and thus the uncertainty for the achievable fidelity. The heat maps in Fig. 4 are intended to serve as a guide for experimentalists working with the silicon vacancy in SiC and considering the benefits of isotopically purifying their samples.

As an extension of the above results, we fit the statistical average of the infidelity shown in Fig. 4(c) using a double-exponential formula. More precisely, we use $\log_{10}(\overline{1-F_{N_R}}) = a_{N_R}e^{b_{N_R}N_B} + c_{N_R}e^{d_{N_R}N_B}$ to fit across each row of Fig. 4(c), where the index $N_R \in [1,10]$ denotes the size of the register and $N_B \in [1,10]$ denotes the size of the

bath. The fitting parameters can be found in Table I, while the data and the fit functions are shown together in Fig. 5. These functions can be used to estimate the average fidelity in the presence of more unwanted spins.

Next, we consider the case of a silicon divacancy defect in SiC with electron spin $S=1$ where the qubit is defined using the $(s_0,s_1)=(0,-1)$ spin states. Similarly to what we showed for the monovacancy center above, in Fig. 6 we show the statistical average of the infidelity and its variance over 100 realizations in a much stronger magnetic field, $B=584$ G, taken from Ref. [11]. Comparing Figs. 6(a) and 4(c), we observe that, despite the difference in the spin states used to define the electronic spin qubit and the strength of the applied magnetic field, the fidelity deteriorates in the same fashion with the size of the register, while it decreases faster with the number of unwanted spins. However, there are cases where the divacancy and a strong magnetic field lead to higher average fidelity; compare, for instance, the $N_B=1$ columns in Figs. 6(a) and 4(c). The

last two features can be attributed to the fact that the combination of total spin $S = 1$ and strong magnetic field lead to resonance times with lower dispersion, hence making it easier for DD pulses to create large registers but more difficult to decouple selected nuclear spins from a large bath. Also, low dispersion in resonance times can affect our ability to create a desired entangled state in the presence of a given number of unwanted spins (see Appendix F).

C. Performance of DD sequences

As a next step, we investigate the suitability of the different DD sequences and the resonance orders versus the total number of nuclear spins. To that end, in Fig. 7(a) we present the probability of a given DD sequence to achieve the highest fidelity. The probability here refers to the number of times that a specific sequence was used in 200 independent realizations. Figure 7(a) shows that UDD$_4$ performs much better for a higher number of qubits and specifically for $N_R \geq 5$ and is the most effective sequence, with probability close to unity, for $N_R \geq 8$. In the same heat map, we see that UDD$_3$ is the preferred DD sequence to use for register sizes $N_R = 1$ and 2, but for large baths, $N_B \geq 6$. Also, CPMG is found to give the best gate fidelity for registers of intermediate size, namely for $N_R \in [2,6]$ and various bath sizes. However, the occurrence probability is not as high, meaning other sequences perform comparably. In Fig. 7(b), we show the probability of a given resonance order to achieve the highest fidelity independently of the DD sequence used. We observe that the first resonance, $k = 1$ (blue tiles), is highly preferred in all sequences; however, the occurrence probability is not considerably high, meaning that the DD sequences perform their best when they have access to a large variety of resonances.

D. Examination of positive gyromagnetic ratio

Finally, we examine the fictitious scenario where the ^{29}Si nuclear spin has positive gyromagnetic ratio, i.e., $\gamma_{^{29}\text{Si}} = +2\pi \times 8.465$ MHz/T. We are interested in this scenario because it will help us conclude whether a mixed bath where the gyromagnetic ratios of the nuclei have opposite signs is preferable over the case where they have the same signs. In Fig. 8 we plot the statistical average of the infidelity and the variance over 100 realizations upon optimization over single-qubit rotations on the electronic spin. We use the same algorithm as in Fig. 4, with the only difference being the sign of $\gamma_{^{29}\text{Si}}$.

Comparing Figs. 4(c) and 4(d) with Figs. 8(a) and 8(b), one can easily see that a mixed nuclear bath with opposite signs in gyromagnetic ratios achieves at least two orders of magnitude lower infidelity for $N_R \leq 5$ and $N_B \leq 4$. Also,

(a)

Register (N_R) \ Bath (N_B)	1	2	3	4	5	6	7	8	9	10
10	1	1	1	1	1	0.99	0.98	0.975	0.97	0.945
9	1	1	0.995	0.995	0.98	0.965	0.935	0.91	0.875	0.845
8	0.99	0.995	0.99	0.96	0.95	0.935	0.85	0.845	0.735	0.695
7	0.985	0.98	0.935	0.92	0.84	0.76	0.685	0.69	0.59	0.48
6	0.88	0.88	0.835	0.725	0.685	0.555	0.49	0.46	0.47	0.53
5	0.745	0.73	0.635	0.47	0.395	0.495	0.59	0.55	0.625	0.61
4	0.58	0.385	0.435	0.52	0.555	0.605	0.6	0.66	0.695	0.66
3	0.41	0.53	0.56	0.615	0.625	0.59	0.665	0.535	0.605	0.575
2	0.635	0.565	0.505	0.48	0.405	0.455	0.535	0.5	0.675	0.605
1	0.58	0.835	0.96	0.97	0.995	0.985	1	0.995	1	0.995

Legend: UDD$_4$ (red), UDD$_3$ (white), CPMG (blue)

(b)

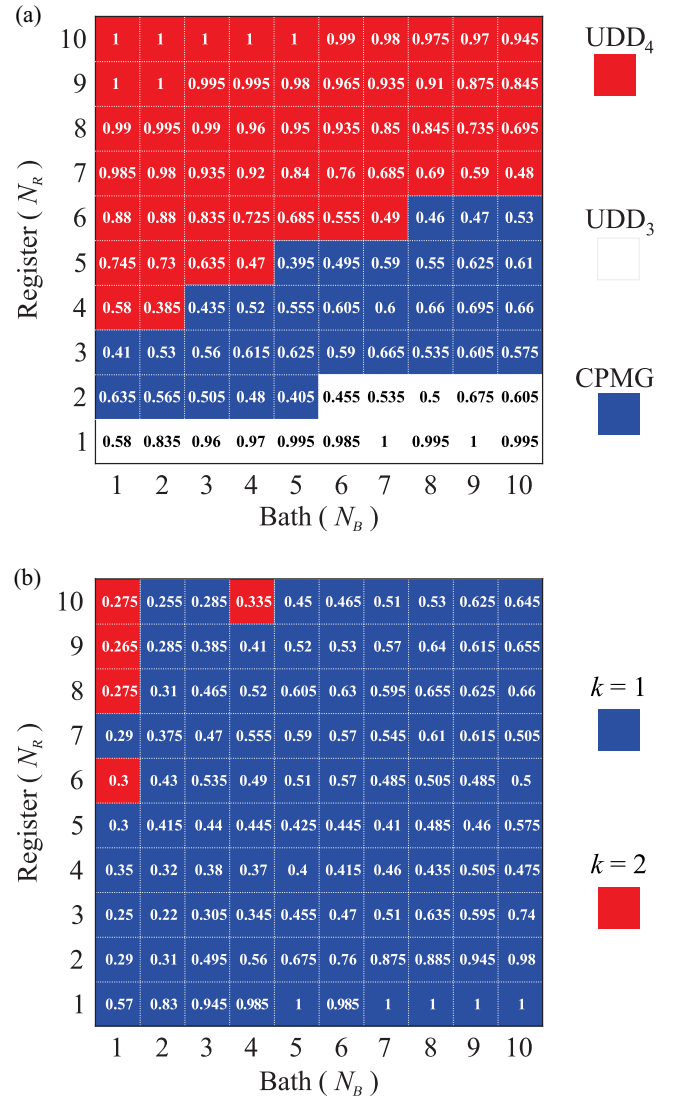| Register (N_R) \ Bath (N_B)	1	2	3	4	5	6	7	8	9	10
10	0.275	0.255	0.285	0.335	0.45	0.465	0.51	0.53	0.625	0.645
9	0.265	0.285	0.385	0.41	0.52	0.53	0.57	0.64	0.615	0.655
8	0.275	0.31	0.465	0.52	0.605	0.63	0.595	0.655	0.625	0.66
7	0.29	0.375	0.47	0.555	0.59	0.57	0.545	0.61	0.615	0.505
6	0.3	0.43	0.535	0.49	0.51	0.57	0.485	0.505	0.485	0.5
5	0.3	0.415	0.44	0.445	0.425	0.445	0.41	0.485	0.46	0.575
4	0.35	0.32	0.38	0.37	0.4	0.415	0.46	0.435	0.505	0.475
3	0.25	0.22	0.305	0.345	0.455	0.47	0.51	0.635	0.595	0.74
2	0.29	0.31	0.495	0.56	0.675	0.76	0.875	0.885	0.945	0.98
1	0.57	0.83	0.945	0.985	1	0.985	1	1	1	1

Legend: $k = 1$ (blue), $k = 2$ (red)

FIG. 7. Best pulse sequence and resonance order versus the size of the bath (unwanted spins) and the size of the register (wanted or target spins). (a) Heat map depicting the most used (or most probable) DD sequence among CPMG (blue), UDD$_3$ (white), and UDD$_4$ (red). (b) Heat map showing the most used (or most probable) resonance order ($k = 1$, blue; $k = 2$, red) used for τ_k. The number in each tile refers to the occurrence probability. In the above simulations, we considered SiC samples with a silicon monovacancy with total spin $S = 3/2$ where the electron qubit is defined by $(s_0, s_1) = (1/2, 3/2)$. The HF values for the ^{13}C and ^{29}Si spins were drawn from uniform distributions in the intervals $2\pi \times [10, 200]$ kHz and $2\pi \times [0.5, 200]$ kHz, respectively. The entangling power threshold was set to $\epsilon_p^{\text{th}} = 0.85$; the magnetic field was $B = 83$ G, leading to Larmor frequencies $(\omega_L^C, \omega_L^{\text{Si}}) = 2\pi \times (88.8797, -70.2595)$ kHz; and the relative abundance was kept constant for all the cases, i.e., ^{29}Si:^{13}C = 4.7%:1.1% = 4.27. Every data point on the heat maps was obtained from 200 realizations, and for each trajectory we kept the combination (τ, N) that resulted in the lowest maximum unwanted one-tangle.
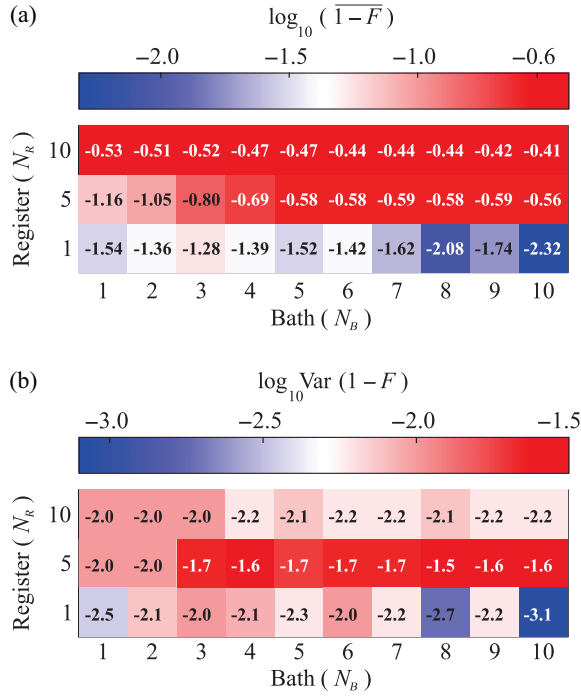
FIG. 8.   Effect of changing the sign of a nuclear gyromagnetic ratio. Gate infidelity $(1 - F)$ versus the size of the bath (unwanted spins) and the size of the register (wanted or target spins) upon optimization over single-qubit rotations on the electronic spin. (a) The decimal logarithm of the statistical average of the infidelity, i.e., $\log_{10}(\overline{1 - F})$. (b) The variance of the infidelity on the same logarithmic scale $\log_{10} \mathrm{Var}(1 - F)$. The number on each tile gives the value of $\log_{10}(\overline{1 - F})$ (a) and $\log_{10} \mathrm{Var}(1 - F)$ (b). In the above simulations, we considered fictitious SiC samples with a silicon monovacancy with total spin $S = 3/2$, and the electron qubit is defined by $(s_0, s_1) = (1/2, 3/2)$. The HF values for the ^{13}C and the ^{29}Si were drawn from uniform distributions in the intervals $2\pi \times [10, 200]$ kHz and $2\pi \times [0.5, 200]$ kHz, respectively. The magnetic field was $B = 83$ G, leading to Larmor frequencies $(\omega_L^C, \omega_L^{Si}) = 2\pi \times (88.8797, 70.2595)$ kHz; and the relative abundance was kept constant for all the cases, i.e., ^{29}Si:^{13}C = 4.7%:1.1% = 4.27. Every data point on the heat maps was obtained from 100 realizations, and for each trajectory we kept the combination (τ, N) that resulted in the lowest maximum unwanted one-tangle.

the performance of opposite signs remains better even in the challenging case of $N_R = 10$ nuclear spins, while the variance is approximately the same. Furthermore, one would expect the two cases to perform approximately the same for $N_R = 1$; however, this is where the differences become most significant. This can be explained by looking at the resonance times, which are larger in the case of negative $\gamma_{29\mathrm{Si}}$ due to the sign difference between the Larmor frequency and the HF values [see Eq. (3)]. Large resonance times lead to more distinct resonances between different nuclear spins, translating to easier decoupling. Overall, the above evidence indicates that a mixed nuclear bath with different signs in the gyromagnetic ratio leads to higher fidelities. It has been previously observed that having two nuclear species is beneficial for coherence times [10,11]; here, we see that it is also beneficial for entangling gates.

V. CONCLUSIONS

Nuclear spins play a crucial role in spin-based solid-state platforms for quantum memories. To fully leverage their potential for creating large-scale quantum networks, a comprehensive investigation of the ability to control nuclear-spin registers in all the promising candidate platforms should be conducted. Here, we developed a method for conducting such a high-throughput sorting of host materials and defects. As a concrete example to showcase our approach, we explored the performance of dynamical decoupling sequences such as CPMG, UDD$_3$, and UDD$_4$ in controlling the nuclear spins surrounding a silicon monovacancy or divacancy defect in SiC. In each case, we quantified the expected performance in terms of the gate infidelity, and found an exponential deterioration not only with the bath size but also with the register size. Additionally, we showed that some sequences perform better on average than others, depending on the register and bath size.

In the pursuit of advancing quantum memory technologies, our work lays a foundation for further exploration. Future research could focus on extending our high-throughput sorting approach to other promising defects and host materials, and on combining it with high-throughput electronic structure calculations. Investigating novel control schemes and pulse sequences, beyond CPMG and UDD, could enhance the performance of quantum memories, enabling more efficient and reliable quantum information processing. In particular, future work could explore leveraging optimal control theory [46] and space-curve quantum control [47], or a combination of these two, to incorporate errors and further optimize the fidelity of entangling gates. Moreover, integrating experimental efforts with theoretical advancements will be essential for moving this field forward. By continuing to push the boundaries of quantum memory research, we can unlock new opportunities for the development of robust and scalable quantum networks.

APPENDIX A: UDD SEQUENCES

For UDD_n sequences, the time intervals between the π pulses are given by

$$q_r = \sin^2\left(\frac{\pi r}{2n+2}\right) - \sin^2\left(\frac{\pi(r-1)}{2n+2}\right), \qquad \text{(A1)}$$

where r takes integer values between 1 and $n+1$, since there are $n+1$ time intervals. It is easy to show that $q_r = q_{n+2-r}$, leading to symmetric time intervals about the halfway point of the sequence. However, this symmetry does not necessarily translate to equal angles of rotation. For UDD_4, $[q_1\tau - \pi - q_2\tau - \pi - q_3\tau - \pi - q_4\tau - \pi - q_5\tau]$, it holds that $\phi_0 \neq \phi_1$.

As mentioned in the main text, UDD_n sequences with odd n (i.e., odd number of π pulses) need to be repeated twice to form a "unit sequence." This stems from the fact that the electron must return to its initial state. So, the UDD_3 unit is given by $[q_1\tau/2 - \pi - q_2\tau/2 - \pi - q_3\tau/2 - \pi - (q_4+q_1)\tau/2 - \pi - q_2\tau/2 - \pi - q_3\tau/2 - \pi - q_4\tau/2]$, where we divided all q_r by a factor of 2 so that the total time adds up to τ.

APPENDIX B: MAKHLIN INVARIANTS

The evolution operator of an electron spin and a lone nuclear spin, given in Eq. (2), can be characterized using the Makhlin invariants [48], commonly denoted by $G_1 \in \mathbb{C}$ and $G_2 \in \mathbb{R}$. These invariants categorize all two-qubit operations into separate entangling categories, ensuring that gates with identical local invariants belong to the same entangling category. This characteristic arises because local operations do not affect the amount of entanglement between the two parties. Gates capable of generating maximal entanglement, known as perfect entanglers, include the controlled NOT (CNOT) and controlled Z (CZ) gates, which are equivalent up to single-qubit rotations. These gates, and any other two-qubit gate locally equivalent to them, define the category of perfect entanglers with $G_1 = 0$ and $G_2 = 1$.

For any given π-pulse sequence repeated N times, the electron-nuclear evolution operator maintains the structure described in Eq. (2), with the only difference being that ϕ_j is now replaced by the total rotation angle $\phi_j(N)$. This specific form of the evolution operator enables us to derive analytical expressions for G_1 and G_2. Understanding these two parameters helps us identify conditions under which the driven electron-nuclear evolution achieves perfect entanglement. Assuming an arbitrary π-pulse sequence and using Eq. (2), we find that G_1 and G_2 as functions of N read

$$G_1 = \left(\cos\frac{\phi_0(N)}{2}\cos\frac{\phi_1(N)}{2} + n_{01}\sin\frac{\phi_0(N)}{2}\sin\frac{\phi_1(N)}{2}\right)^2,$$
$$\text{(B1a)}$$

$$G_2 = 1 + n_{01}\sin\phi_0(N)\sin\phi_1(N)$$
$$+ 2\left(\cos^2\frac{\phi_0(N)}{2}\cos^2\frac{\phi_1(N)}{2}\right.$$
$$\left. + n_{01}^2\sin^2\frac{\phi_0(N)}{2}\sin^2\frac{\phi_1(N)}{2}\right), \qquad \text{(B1b)}$$

where $n_{01} \equiv \mathbf{n}_0 \cdot \mathbf{n}_1$, $G_1 \in [0,1]$, and $G_2 \in [1,3]$.

These intervals reveal that π-pulse sequences can create perfect entangling gates only within the CNOT equivalence class, where $(G_1, G_2) = (0, 1)$. When the resonance condition is met, i.e., $n_{01} = -1$, we have $G_1 = \cos^2([\phi_0(N) + \phi_1(N)]/2)$. Enforcing $G_1 = 0$ determines the required number of sequence iterations N for achieving the wanted controlled gate. To estimate N, knowledge of the rotation angles in a single iteration suffices. The minima of G_1 occur at $N = (2k+1)\pi/(\phi_0 + \phi_1)$; however, N is an integer and so the value of this expression must be rounded in general. Notice that G_1 can also be zero for other N values, provided that $\mathbf{n}_0 \cdot \mathbf{n}_1 \leq 0$.

APPENDIX C: QUANTIFYING ROBUSTNESS UNDER PULSE ERRORS

Although DD sequences have been used experimentally for over a decade in spin platforms, and pulse fidelity has reached a mature level exceeding 99% [49–51], it remains essential to examine their robustness under realistic experimental imperfections. References [52,53] showed that the π-pulse errors can be well approximated as static errors. Here, we will consider static as well as random π-pulse errors, and study these imperfections using the CPMG or XY2 sequences. These errors can, in principle, cause over- or under-rotations, illustrating the impact on sequence performance to achieve high-fidelity gates.

Figure 9 captures the robustness of CPMG and XY2 sequences under static and stochastic errors, comparing the maximum one-tangle in the bath, ϵ_p, and the gate fidelity, F, against error-free conditions. In detail, we observe that, even for 1% systematic over-rotations, the performance of CPMG deteriorates significantly, dropping the fidelity to 0.918 and 0.8 for configurations I and II, respectively. The performance becomes worse when pulses systematically over-rotate the defect by 2%, reaching 0.43 in configuration II. On the other hand, XY2 sequences reveal their capability to cancel the systematic errors to some extent by retaining the fidelity over 0.998 even for 2% error in pulses. However, the landscape is inverted in the case where the error in each π pulse follows a uniform distribution, $U(-2\%, 2\%)$, allowing errors to range from -2% to 2%. In this case, while both CPMG and XY2 maintain comparable average decoupling effectiveness, CPMG displays a slight advantage in average performance over XY2, albeit with a larger variance.
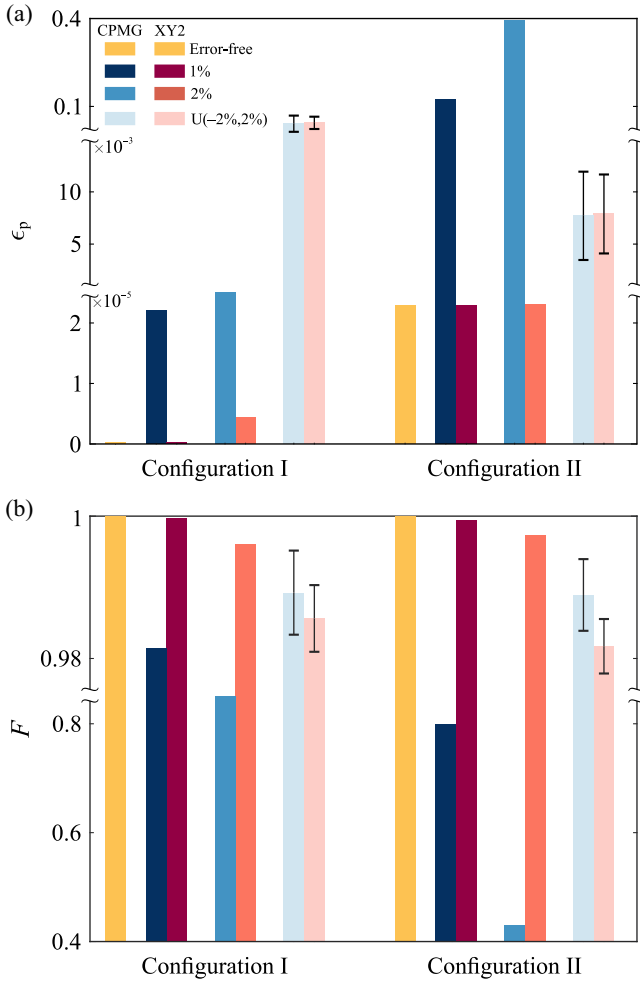
FIG. 9. Scaled one-tangles and fidelity in the presence of pulse errors. (a) Maximum bath ϵ_p and (b) gate fidelity for the error-free, systematic over-rotation errors of 1% and 2%, and uniformly distributed errors case, U$(-2\%, 2\%)$; see key for colors. In the ideal case, CPMG and XY2 have precisely the same performance. The blue palette refers to CPMG pulses while the red palette to XY2, in both panels (a) and (b). For randomly distributed errors, we plot the average over 100 realizations of maximum ϵ_p in panel (a) and fidelity in panel (b), and the error bars represent one standard deviation. The data for configurations I and II are taken from the ideal case shown in Figs. 3(b) and 3(c), respectively.

The above results reveal that, for small error rates that align with state-of-the-art experimental standards, the one-tangle metric shows minimal sensitivity, indicating that our method can be readily applied under these conditions. This stability suggests that the approach can effectively handle realistic pulse fidelities encountered in current experiments.

The above analysis can be further expanded by exploring additional DD sequences to compare their robustness against systematic and stochastic errors. Including other realistic imperfections, such as pulse timing jitter, would allow for a more comprehensive evaluation of the resilience of these sequences under practical experimental conditions. This approach would provide a broader insight into optimizing sequence design for high-fidelity gate performance in quantum memory applications.

APPENDIX D: ALGORITHMIC PROCEDURE FOR EFFICIENT SPIN-QUBIT ASSESSMENT

Here we provide the pseudocode we developed to obtain the results shown in most of the figures. The pseudocode is given below.

1: **Input parameters:** $(A_{||}, A_\perp)$ for each nuclear spin, $R :=$ # of register spins, $B :=$ # of bath spins, eone-tangle threshold ϵ_p^{th}, maximum gate time T_g, set time window $\delta\tau$

2: **for** each nuclear spin l **do**

3:     **for** each resonance k **do**

4:         compute $\tau_k^{(l)}$

5:         refine $\tau_k^{(l)}$ s.t. $(\mathbf{n}_0 \cdot \mathbf{n}_1)^{(l)} = -1$

6:         **for** $\tau \in [\tau_k^{(l)} - \delta\tau, \tau_k^{(l)} + \delta\tau]$ **do**

7:             **while** $N\tau \leq T_g$ **do**

8:                 compute $\epsilon_p^{\text{th}}(\tau, N)$

9:                 **if** $\epsilon_p^{\text{th}}(\tau, N) \geq \epsilon_p^{\text{th}}$ **then**

10:                     spin is part of the register

11:                 **else**

12:                     spin is part of the bath

13: Choose (τ, N) s.t. the maximum one-tangle of bath spins is minimized, and the number of spins in the register and the bath are (R, N) as definided at the begining.

14: Use Eq. (16) to optimize gate fidelity up to local operations on the electronic spin

APPENDIX E: GATE FIDELITY OPTIMIZATION

As shown in the main text, to optimize the gate fidelity up to local operations on the electronic spin, we define the target evolution operator as

$$\tilde{U}_0 = R_{\mathbf{n}^e}(\theta) U_0 = \sum_{j=0,1} (R_{\mathbf{n}^e}(\theta)\sigma_{jj}) \bigotimes_{k=1}^{K} R_{\mathbf{n}_j^{(k)}}(\phi_j^{(k)}), \quad \text{(E1)}$$

where $R_{\mathbf{n}^e}(\theta) = e^{-i(\theta/2)\boldsymbol{\sigma}\cdot\mathbf{n}^e}$ is the rotation matrix around axis $\mathbf{n}^e$ acting on the electronic spin. Next, we substitute Eqs. (E1) and (14) into Eq. (13) to obtain
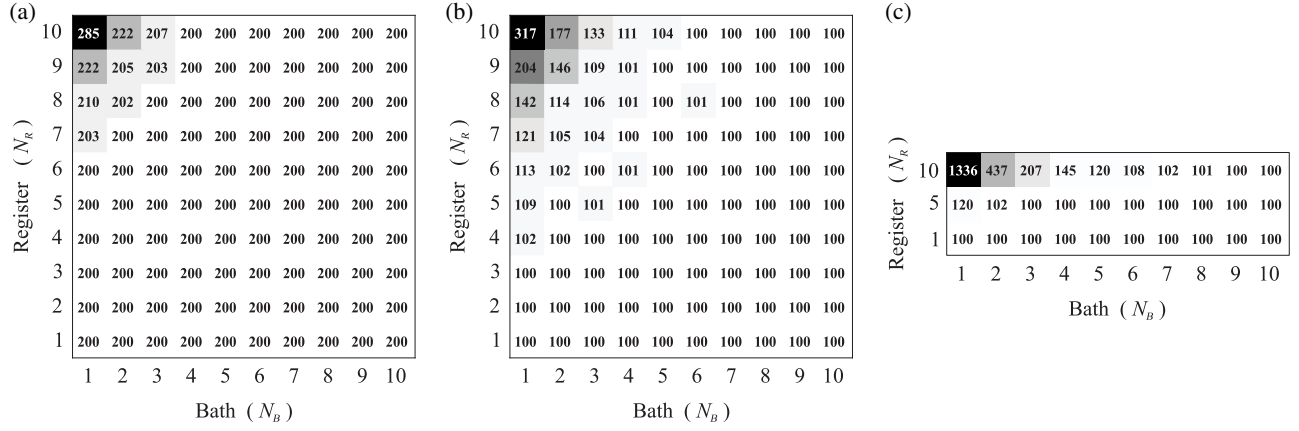
FIG. 10.   Total number of realizations simulated to obtain the results presented in the main text. Total number of realizations for (a) a silicon monovacancy defect in SiC, (b) a divacancy, and (c) a monovacancy in the fictitious nuclear-spin bath where $\gamma_{^{29}\mathrm{Si}} > 0$. The successful realizations for panels (a), (b), and (c) were 200, 100, and 100, respectively.

$$
\begin{aligned}
F &= \frac{1}{d(d+1)} \left[\mathrm{tr}\left[\sum_{k=1}^{2^{L-K}} E_k^\dagger E_k \right] + \sum_{k=1}^{2^{L-K}} \left|\mathrm{tr}[\tilde{U}_0^\dagger E_k]\right|^2 \right] = \frac{1}{d(d+1)} \left[d + \sum_k \left|\mathrm{tr}\left[\sum_j c_j^{(k)} p_j^{(k)} R_{\mathbf{n}^e}^\dagger(\theta) \sigma_{jj} \otimes \mathbb{1}_{2^K \times 2^K} \right]\right|^2 \right] \\
&= \frac{1}{d(d+1)} \left[d + \sum_k \left|\mathrm{tr}\left[\sum_j c_j^{(k)} p_j^{(k)} R_{\mathbf{n}^e}^\dagger(\theta) \sigma_{jj} \right]\mathrm{tr}[\mathbb{1}_{2^K \times 2^K}]\right|^2 \right] \\
&= \frac{1}{d(d+1)} \left[2^{K+1} + 2^{2K} \sum_k \left|\mathrm{tr}\left[\sum_j c_j^{(k)} p_j^{(k)} R_{\mathbf{n}^e}^\dagger(\theta) \sigma_{jj} \right]\right|^2 \right] \\
&= \frac{1}{2^{K+1}+1} \left[1 + 2^{K-1} \sum_k \left|\mathrm{tr}\left[\sum_j c_j^{(k)} p_j^{(k)} R_{\mathbf{n}^e}^\dagger(\theta) \sigma_{jj} \right]\right|^2 \right] \\
&= \frac{1}{2^{K+1}+1} \left[1 + 2^{K-1} \sum_k \left| \sum_{j=0,1} c_j^{(k)} p_j^{(k)} \left\{ \cos(\theta/2) + i(-1)^j \sin(\theta/2) n_z^e \right\} \right|^2 \right].
\end{aligned}
\tag{E2}
$$

Here we have used the fact that $\tilde{U}_0$ is a $2^{K+1} \times 2^{K+1}$ unitary gate, the Kraus operators E_k have dimensions of $2^{K+1} \times 2^{K+1}$, the trace property $\mathrm{tr}[A \otimes B] = \mathrm{tr}[A]\mathrm{tr}[B]$, and in the end the fact that $\sigma_{jj} = |j\rangle\langle j|$ is a projector. Also, $c_j^{(k)}$ and $p_j^{(k)}$ are given in the main text.

APPENDIX F: SUCCESS PROBABILITY

Here we present the total number of realizations we had to simulate to obtain the successful realizations used in the figures in the main text. As a successful realization, we define a realization in which we can find a DD

sequence (CPMG or UDD) and a pair of pulse parameters (τ, N) such that a desired number of N_R nuclear spins have $\epsilon_p \geq \epsilon_p^{\mathrm{th}}$ and a desired number of N_B unwanted spins have $\epsilon_p < \epsilon_p^{\mathrm{th}}$. Any other realization is considered unsuccessful and we stop the simulation. For instance, we have an unsuccessful realization even in the case where the HF couplings are such that we cannot create a register of N_R spins surrounded by a bath of N_B spins, but we may be able to create a register of $N_R - k$ spins surrounded by $N_B + k$ spins (where k is an integer).

In Fig. 10 we show the total number of realizations needed for the silicon monovacancy, the divacancy, and the

fictitious case of positive $\gamma_{29\text{Si}}$, where it becomes clear that the monovacancy in a low magnetic field has the highest success rate, while the fictitious bath leads to the lowest success rate. Furthermore, it becomes evident that the $(N_R, N_B) = (10, 1)$ combination is the most challenging for all the cases, and especially for the fictitious one. However, except for the top left corner in the heat maps, the success rate for all the other combinations is always equal to unity.

---

[1] M. Pompili, S. L. N. Hermans, S. Baier, H. K. C. Beukers, P. C. Humphreys, R. N. Schouten, R. F. L. Vermeulen, M. J. Tiggelman, L. dos Santos Martins, B. Dirkse, S. Wehner, and R. Hanson, Realization of a multinode quantum network of remote solid-state qubits, Science **372**, 259 (2021).

[2] H. Bernien, B. Hensen, W. Pfaff, G. Koolstra, M. S. Blok, L. Robledo, T. H. Taminiau, M. Markham, D. J. Twitchen, L. Childress, and R. Hanson, Heralded entanglement between solid-state qubits separated by three metres, Nature **497**, 86 (2013).

[3] N. Kalb, A. A. Reiserer, P. C. Humphreys, J. J. W. Bakermans, S. J. Kamerling, N. H. Nickerson, S. C. Benjamin, D. J. Twitchen, M. Markham, and R. Hanson, Entanglement distillation between solid-state quantum network nodes, Science **356**, 928 (2017).

[4] C. Nguyen, D. Sukachev, M. Bhaskar, B. Machielse, D. Levonian, E. Knall, P. Stroganov, R. Riedinger, H. Park, M. Lončar, and M. Lukin, Quantum network nodes based on diamond qubits with an efficient nanophotonic interface, Phys. Rev. Lett. **123**, 183602 (2019).

[5] C. T. Nguyen, D. D. Sukachev, M. K. Bhaskar, B. Machielse, D. S. Levonian, E. N. Knall, P. Stroganov, C. Chia, M. J. Burek, R. Riedinger, H. Park, M. Lončar, and M. D. Lukin, An integrated nanophotonic quantum register based on silicon-vacancy spins in diamond, Phys. Rev. B **100**, 165428 (2019).

[6] A. E. Rugar, S. Aghaeimeibodi, D. Riedel, C. Dory, H. Lu, P. J. McQuade, Z.-X. Shen, N. A. Melosh, and J. Vučković, Quantum photonic interface for tin-vacancy centers in diamond, Phys. Rev. X **11**, 031021 (2021).

[7] T. Iwasaki, Y. Miyamoto, T. Taniguchi, P. Siyushev, M. H. Metsch, F. Jelezko, and M. Hatano, Tin-vacancy quantum emitters in diamond, Phys. Rev. Lett. **119**, 253601 (2017).

[8] C. Babin *et al.*, Fabrication and nanophotonic waveguide integration of silicon carbide colour centres with preserved spin-optical coherence, Nat. Mater. **21**, 67 (2021).

[9] R. Nagy, M. Niethammer, M. Widmann, Y.-C. Chen, P. Udvarhelyi, C. Bonato, J. U. Hassan, R. Karhu, I. G. Ivanov, N. T. Son, J. R. Maze, T. Ohshima, O. O. Soykal, A. Gali, S.-Y. Lee, F. Kaiser, and J. Wrachtrup, High-fidelity spin and optical control of single silicon-vacancy centres in silicon carbide, Nat. Commun. **10**, 1954 (2019).

[10] M. Widmann, S.-Y. Lee, T. Rendler, N. T. Son, H. Fedder, S. Paik, L.-P. Yang, N. Zhao, S. Yang, I. Booker, A. Denisenko, M. Jamali, S. A. Momenzadeh, I. Gerhardt, T. Ohshima, A. Gali, E. Janzén, and J. Wrachtrup, Coherent control of single spins in silicon carbide at room temperature, Nat. Mater. **14**, 164 (2014).

[11] A. Bourassa, C. P. Anderson, K. C. Miao, M. Onizhuk, H. Ma, A. L. Crook, H. Abe, J. Ul-Hassan, T. Ohshima, N. T. Son, G. Galli, and D. D. Awschalom, Entanglement and control of single nuclear spins in isotopically engineered silicon carbide, Nat. Mater. **19**, 1319 (2020).

[12] A. Alkauskas, L. C. Bassett, A. L. Exarhos, and K.-M. C. Fu, Defects by design: Quantum nanophotonics in emerging materials, Nanophotonics **8**, 1863 (2019).

[13] D. Broberg, K. Bystrom, S. Srivastava, D. Dahliah, B. A. D. Williamson, L. Weston, D. O. Scanlon, G.-M. Rignanese, S. Dwaraknath, J. Varley, K. A. Persson, M. Asta, and G. Hautier, High-throughput calculations of charged point defect properties with semi-local density functional theory—Performance benchmarks for materials screening applications, Npj Comput. Mater. **9**, 72 (2023).

[14] H.-J. Briegel, W. Dür, J. I. Cirac, and P. Zoller, Quantum repeaters: The role of imperfect local operations in quantum communication, Phys. Rev. Lett. **81**, 5932 (1998).

[15] S. Brand, T. Coopmans, and D. Elkouss, in *OSA Quantum 2.0 Conference*, QUANTUM (Optica Publishing Group, Washington, DC United States, 2020).

[16] L. Bergeron, C. Chartrand, A. T. K. Kurkjian, K. J. Morse, H. Riemann, N. V. Abrosimov, P. Becker, H.-J. Pohl, M. L. W. Thewalt, and S. Simmons, Silicon-integrated telecommunications photon-spin interface, PRX Quantum **1**, 020301 (2020).

[17] G. Waldherr, Y. Wang, S. Zaiser, M. Jamali, T. Schulte-Herbrüggen, H. Abe, T. Ohshima, J. Isoya, J. F. Du, P. Neumann, and J. Wrachtrup, Quantum error correction in a solid-state hybrid spin register, Nature **506**, 204 (2014).

[18] M. H. Abobeih, J. Randall, C. E. Bradley, H. P. Bartling, M. A. Bakker, M. J. Degen, M. Markham, D. J. Twitchen, and T. H. Taminiau, Atomic-scale imaging of a 27-nuclear-spin cluster using a quantum sensor, Nature **576**, 411 (2019).

[19] G. L. van de Stolpe, D. P. Kwiatkowski, C. E. Bradley, J. Randall, M. H. Abobeih, S. A. Breitweiser, L. C. Bassett, M. Markham, D. J. Twitchen, and T. H. Taminiau, Mapping a 50-spin-qubit network through correlated sensing, Nat. Commun. **15**, 2006 (2024).

[20] V. Giovannetti, S. Lloyd, and L. Maccone, Quantum-enhanced measurements: Beating the standard quantum limit, Science **306**, 1330 (2004).

[21] S. Zaiser, T. Rendler, I. Jakobi, T. Wolf, S.-Y. Lee, S. Wagner, V. Bergholm, T. Schulte-Herbrüggen, P. Neumann, and J. Wrachtrup, Enhancing quantum sensing sensitivity by a quantum memory, Nat. Commun. **7**, 12279 (2016).

[22] T. H. Taminiau, J. J. T. Wagenaar, T. van der Sar, F. Jelezko, V. V. Dobrovitski, and R. Hanson, Detection and control of individual nuclear spins using a weakly coupled electron spin, Phys. Rev. Lett. **109**, 137602 (2012).

[23] T. H. Taminiau, J. Cramer, T. van der Sar, V. V. Dobrovitski, and R. Hanson, Universal control and error correction in multi-qubit spin registers in diamond, Nat. Nanotechnol. **9**, 171 (2014).

[24] C. E. Bradley, J. Randall, M. H. Abobeih, R. C. Berrevoets, M. J. Degen, M. A. Bakker, M. Markham, D. J. Twitchen,

and T. H. Taminiau, A ten-qubit solid-state spin register with quantum memory up to one minute, Phys. Rev. X **9**, 031045 (2019).

[25] P. C. Humphreys, N. Kalb, J. P. J. Morits, R. N. Schouten, R. F. L. Vermeulen, D. J. Twitchen, M. Markham, and R. Hanson, Deterministic delivery of remote entanglement on a quantum network, Nature **558**, 268 (2018).

[26] J. Cramer, N. Kalb, M. A. Rol, B. Hensen, M. S. Blok, M. Markham, D. J. Twitchen, R. Hanson, and T. H. Taminiau, Repeated quantum error correction on a continuously encoded qubit by real-time feedback, Nat. Commun. **7**, 11526 (2016).

[27] M. H. Abobeih, Y. Wang, J. Randall, S. J. H. Loenen, C. E. Bradley, M. Markham, D. J. Twitchen, B. M. Terhal, and T. H. Taminiau, Fault-tolerant operation of a logical qubit in a diamond quantum processor, Nature **606**, 884 (2022).

[28] C. M. Knaut, A. Suleymanzade, Y. C. Wei, D. R. Assumpcao, P. J. Stas, Y. Q. Huan, B. Machielse, E. N. Knall, M. Sutula, G. Baranes, N. Sinclair, C. De-Eknamkul, D. S. Levonian, M. K. Bhaskar, H. Park, M. Lončar, and M. D. Lukin, Entanglement of nanophotonic quantum memory nodes in a telecom network, Nature **629**, 573 (2024).

[29] E. Takou, E. Barnes, and S. E. Economou, Precise control of entanglement in multinuclear spin registers coupled to defects, Phys. Rev. X **13**, 011004 (2023).

[30] H. Y. Carr and E. M. Purcell, Effects of diffusion on free precession in nuclear magnetic resonance experiments, Phys. Rev. **94**, 630 (1954).

[31] S. Meiboom and D. Gill, Modified spin-echo method for measuring nuclear relaxation times, Rev. Sci. Instrum. **29**, 688 (1958).

[32] G. de Lange, Z. H. Wang, D. Ristè, V. V. Dobrovitski, and R. Hanson, Universal dynamical decoupling of a single solid-state spin from a spin bath, Science **330**, 60 (2010).

[33] G. S. Uhrig, Keeping a quantum bit alive by optimized π-pulse sequences, Phys. Rev. Lett. **98**, 100504 (2007).

[34] C. Bradley, Ph.D. thesis, TU Delft, 2021.

[35] L. M. K. Vandersypen and I. L. Chuang, NMR techniques for quantum control and computation, Rev. Mod. Phys. **76**, 1037 (2005).

[36] A. J. Freeman and R. B. Frankel, *Hyperfine Interactions* (Academic Press, New York, 1967).

[37] W. Dong, F. A. Calderon-Vargas, and S. E. Economou, Precise high-fidelity electron–nuclear spin entangling gates in NV centers via hybrid dynamical decoupling sequences, New J. Phys. **22**, 073059 (2020).

[38] T. Linowski, G. Rajchel-Mieldzioć, and K. Życzkowski, Entangling power of multipartite unitary gates, J. Phys. A: Math. Theor. **53**, 125303 (2020).

[39] P. Zanardi, C. Zalka, and L. Faoro, Entangling power of quantum evolutions, Phys. Rev. A **62**, 030301 (2000).

[40] S. Balakrishnan and R. Sankaranarayanan, Entangling power and local invariants of two-qubit gates, Phys. Rev. A **82**, 034301 (2010).

[41] V. Coffman, J. Kundu, and W. K. Wootters, Distributed entanglement, Phys. Rev. A **61**, 052306 (2000).

[42] M. A. Nielsen and I. L. Chuang, *Quantum Computation and Quantum Information* (Cambridge University Press, Cambridge, England, 2010).

[43] J. R. Maze, A. Dréau, V. Waselowski, H. Duarte, J.-F. Roch, and V. Jacques, Free induction decay of single spins in diamond, New J. Phys. **14**, 103041 (2012).

[44] G.-Q. Liu, X.-Y. Pan, Z.-F. Jiang, N. Zhao, and R.-B. Liu, Controllable effects of quantum fluctuations on spin free-induction decay at room temperature, Sci. Rep. **2**, 432 (2012).

[45] K. Ghosh, H. Ma, M. Onizhuk, V. Gavini, and G. Galli, Spin–spin interactions in defects in solids from mixed all-electron and pseudopotential first-principles calculations, Npj Comput. Mater. **7**, 123 (2021).

[46] C. P. Koch, U. Boscain, T. Calarco, G. Dirr, S. Filipp, S. J. Glaser, R. Kosloff, S. Montangero, T. Schulte-Herbrüggen, D. Sugny, and F. K. Wilhelm, Quantum optimal control in quantum technologies. Strategic report on current status, visions and goals for research in Europe, EPJ Quantum Technol. **9**, 19 (2022).

[47] E. Barnes, F. A. Calderon-Vargas, W. Dong, B. Li, J. Zeng, and F. Zhuang, Dynamically corrected gates from geometric space curves, Quantum Sci. Technol. **7**, 023001 (2022).

[48] Y. Makhlin, Nonlocal properties of two-qubit gates and mixed states, and the optimization of quantum computations, Quantum Information Processing **1**, 243 (2002).

[49] B. Naydenov, F. Dolde, L. T. Hall, C. Shin, H. Fedder, L. C. L. Hollenberg, F. Jelezko, and J. Wrachtrup, Dynamical decoupling of a single-electron spin at room temperature, Phys. Rev. B **83**, 081201 (2011).

[50] Z.-H. Wang, W. Zhang, A. M. Tyryshkin, S. A. Lyon, J. W. Ager, E. E. Haller, and V. V. Dobrovitski, Effect of pulse error accumulation on dynamical decoupling of the electron spins of phosphorus donors in silicon, Phys. Rev. B **85**, 085206 (2012).

[51] L. Zaporski, N. Shofer, J. H. Bodey, S. Manna, G. Gillard, M. H. Appel, C. Schimpf, S. F. Covre da Silva, J. Jarman, G. Delamare, G. Park, U. Haeusler, E. A. Chekhovich, A. Rastelli, D. A. Gangloff, M. Atatüre, and C. Le Gall, Ideal refocusing of an optically active spin qubit under strong hyperfine interactions, Nat. Nanotechnol. **18**, 257 (2023).

[52] G. D. Lange, Ph.D. thesis, TU Delft, 2012, available at https://resolver.tudelft.nl/uuid:7e730d04-c04c-404f-a2a8-4a8e62a99823.

[53] T. van der Sar, Ph.D. thesis, TU Delft, 2012, available at https://resolver.tudelft.nl/uuid:c8b7eb3d-2e42-4357-ba96-4bef1f352aac.